Distinct and interdependent functions of three RING proteins regulate recombination during mammalian meiosis

Masaru Ito[1,2,5,*], Yan Yun[1,2], Dhananjaya S. Kulkarni[1,2], Sunkyung Lee[1,2], Sumit Sandhu[1,2], Briana Nuñez[1,3], Linya Hu[2], Kevin Lee[2], Nelly Lim[2], Rachel M. Hirota[2], Rowan Prendergast[2], Cynthia Huang[2], Ivy Huang[2] and Neil Hunter[1,2,4,6,*]

[1]Howard Hughes Medical Institute, University of California Davis, Davis, CA 95616, USA

[2]Department of Microbiology & Molecular Genetics, University of California Davis, Davis, CA 95616, USA

[3]Department of Biochemistry & Molecular Biology, Brown University, Providence, RI 02912, USA

[4]Department of Molecular & Cellular Biology, University of California Davis, Davis, CA 95616, USA

[5]Current address: Institute for Protein Research, Osaka University, Osaka 565-0871, Japan

[6]Lead contact: nhunter@ucdavis.edu (N.H.)

[*]Correspondence: msrito2@protein.osaka-u.ac.jp (M.I.), nhunter@ucdavis.edu (N.H.)

Classification: CELL BIOLOGY

Keywords: fertility, meiosis, gamete, crossing over, recombination, aneuploidy, chromosome segregation, DNA repair

SUMMARY

During meiosis, each pair of homologous chromosomes becomes connected by at least one crossover, as required for accurate segregation at the first division, and adjacent crossovers are widely separated thereby limiting total numbers. In coarsening models, crossover patterning results from nascent recombination sites competing to accrue a limiting pro-crossover RING-domain protein (COR) that diffuses between synapsed chromosomes. Here we delineate the localization dynamics of three mammalian CORs in mouse and determine their interdependencies. RNF212, HEI10 and a new member RNF212B show divergent spatiotemporal dynamics along synapsed chromosomes, including profound differences in spermatocytes and oocytes, that are not easily reconciled by elementary coarsening models. Contrasting mutant phenotypes and genetic requirements indicate that RNF212B, RNF212, and HEI10 play distinct but interdependent functions in regulating meiotic recombination and

coordinating the events of meiotic prophase-I by integrating signals from DNA breaks, homolog synapsis, the cell-cycle, and incipient crossover sites.

SIGNIFICANCE

Meiosis produces haploid gametes by precisely halving the chromosome complement. Crossing over between homologous chromosomes (homologs) is essential for their accurate segregation and defects are associated with infertility, miscarriage, and congenital disease. Factors that ensure crossing over between each pair of homologs include mammalian RING-domain proteins RNF212, HEI10, and RNF212B, alleles of which are linked to infertility and heritable variation in crossover rate. This study focuses on understanding the functions and relationships between pro-crossover RING proteins (CORs) in mouse, providing important insights into their roles in regulating recombination, the DNA repair process that gives rise to crossovers. Notably, chromosomal localization dynamics of the three CORs are distinct and show striking sexual dimorphism with important implications for models of crossover control.

INTRODUCTION

49 During sexual reproduction, parents contribute equally to their offspring by producing gametes
50 with precisely half the normal cellular ploidy. This is achieved via the two successive rounds of
51 chromosome segregation that occur during meiosis. Accurate segregation during the first
52 meiotic division (MI) requires crossing over between each pair of homologous chromosomes
53 (homologs). In combination with cohesion between sister-chromatids, crossovers create
54 connections called chiasmata that enable the stable biorientation of homolog pairs on the
55 meiosis-I spindle [1-3]. Defective crossing over can trigger cell death via the spindle checkpoint [4],
56 or cause aneuploidy due to chromosome missegregation [5, 6], and is therefore associated with
57 infertility, miscarriage, and congenital syndromes such as Down, Turner and Klinefelter [7-10].
58
59 Crossing over is typically the minority outcome of meiotic recombination with most events being
60 repaired as noncrossovers without exchange of chromosome arms; for example, in mouse
61 spermatocytes only ~24 crossovers are selected from ~250 recombination events initiated by
62 programmed DNA double-strand breaks (DSBs) [11]. Crossover sites are selected in such a way
63 that each pair of chromosomes almost always obtains at least one crossover, termed crossover
64 assurance; adjacent events tend to be widely and evenly spaced via crossover interference

65 (which also limits total crossovers); and crossover numbers per nucleus show low variance

66 relative to DSBs, a buffering process known as crossover homeostasis [2, 3, 12]. The molecular

67 basis of crossover patterning remains unclear but manifests at the cytological level as the

68 selective retention/accumulation of certain pro-crossover factors at designated crossover sites

69 as prophase progresses [2, 3]. Among these are RING-domain proteins related to budding yeast

70 Zip3 [13], inferred to mediate protein modification by ubiquitin and the related small-protein

71 modifier SUMO [2, 14-21]. Species differ with respect to the number and subgroup (Zip3/RNF212

72 and HEI10) of these **C**ross**O**ver **R**ING proteins (CORs). For example, *Sordariales* and plant

73 genomes encode a single HEI10 homolog [13, 18, 22]; *Drosophila* encodes three Zip3/RNF212-like

74 proteins, two of which appear to be redundant [23 21]; and *C. elegans* has four members with

75 homology to both subgroups [19, 20, 24].

76

77 Mammalian genomes encode both RNF212 and HEI10 (a.k.a. CCNBIP1) homologs with

78 interrelated functions that are essential for crossing over [15-17, 25]. RNF212 specifically localizes

79 between synapsed chromosomes, initially as numerous small foci all along the central region of

80 synaptonemal complexes (SCs), before undergoing HEI10-dependent repatterning to

accumulate at prospective crossover sites while being lost elsewhere [15-17]. RNF212 and other CORs are inferred to stabilize pro-crossover factors that directly mediate the DNA events of crossing over [15-19, 26, 27]. These include the MutSγ complex, a heterodimer of MSH4 and MSH5 that can bind D-loop and Holliday junction intermediates [28-30], and is inferred to stabilize and protect them from dissociation by the conserved Bloom-helicase/decatenase complex, BLM-TOPIIIα-RMI1-RMI2 (analogous to Sgs1-Top3-Rmi1 in budding yeast)[31-34]. In mouse spermatocytes, MutSγ initially localizes to a majority of recombination sites during late zygotene and early pachytene as homologs complete synapsis [11, 15]. Subsequently, MutSγ is lost from most sites but retained at prospective crossover sites, which then accumulate crossover-specific factors such as the MutLγ endonuclease [2, 29].

A key question for understanding meiotic crossover control is whether the dynamic focal patterning of COR proteins along SCs is responsible for specifying crossover sites, as proposed by recent models that invoke phase-transition/condensation, coarsening, and/or Ostwald ripening processes [19, 35-37]. In these models, adjacent recombination sites compete to accumulate a limiting amount of COR protein that diffuses along synaptonemal complexes, with

97 crossover designation ensuing at “winning” sites where COR has been accrued. Alternatively,
98 COR patterning may occur as a downstream consequence of crossover patterning by a distinct
99 process such as the mechanical stress envisioned in the beam-film model [38 39]. The latter
100 possibility does not exclude COR coarsening, which could help reinforce initial crossover
101 designation or have other downstream functions.
102
103 Here we characterize mammalian CORs RNF212, HEI10, and a new member RNF212B [40-45].
104 Contrasting phenotypes, localization, and genetic dependencies imply that RNF212B, RNF212,
105 and HEI10 function as distinct modules that integrate signals from DSBs, synapsis, the cell-
106 cycle, and developing crossover complexes in order to effect the spatiotemporal coordination of
107 the major events of meiotic prophase-I. Moreover, the three CORs show diverse spatiotemporal
108 dynamics, including striking differences between males and females, features that are not
109 readily reconciled by coarsening models of crossover patterning.
110
111
112 **RESULTS**

113 ***Rnf212b*$^{-/-}$ mutant mice are sterile due to diminished crossing over**

114 Null mutations in mouse *Rnf212b* were created by pronuclear injection with CRISPR-Cas9,

115 targeting sequences immediately downstream of the first ATG (**Figures S1** and **S2**). Seven

116 mutated lines were obtained, the mutations and phenotypes of which are summarized in **Table**

117 **S1**. Two identical mutant lines, with a single nucleotide insertion that results in a frameshift after

118 the eighth codon and a premature stop codon after just 27 codons (**Figure S2B**), were chosen

119 for detailed phenotypic analysis. An independent *Rnf212b* mutant mouse line was recently

120 reported with similar phenotypes to those described below [45].

121

122 Heterozygous mutant animals were backcrossed four times and then bred to homozygosity.

123 Mature *Rnf212b*$^{-/-}$ mutant males had testes that were ~3-fold smaller than wild-type counterparts

124 (means ± SDs of 219.8 ± 16.8 mg per pair of testes from 8 wild-type mice versus 71.6 ± 7.8 mg

125 from 6 *Rnf212b*$^{-/-}$ mice; $p < 0.0001$, two-tailed *t* test; **Figure 1A**), the cauda epididymides were

126 devoid of sperm, and the animals were sterile. Testis sections from *Rnf212b*$^{-/-}$ mutant males

127 revealed that post-metaphase-I stages and spermatozoa were absent indicating loss of

128 spermatocytes at stage XII (**Figure 1B**). Sterility was also observed for female *Rnf212b*$^{-/-}$

129 mutants, analysis of which is presented in **Figure 6**.

130

131 *Rnf212*$^{-/-}$ mutants are sterile because crossing over almost completely fails, resulting in

132 unconnected univalent chromosomes at metaphase I [15]. To determine whether this is also the

133 case for *Rnf212b*$^{-/-}$ mutants, chromosome spreads from diakinesis/metaphase-I spermatocytes

134 were analyzed (**Figure 1C**). In wild-type nuclei, all autosomes presented as bivalents with 24.1

135 ± 2.3 chiasmata per nucleus (mean ± SD; *n* = 61 nuclei). Conversely, *Rnf212b*$^{-/-}$ nuclei

136 contained primarily univalents with a residual of 1-3 chiasmata (mean ± SD; 0.66 ± 0.75

137 chiasmata, *n* = 77 nuclei). Immunostaining of surface-spread pachytene-stage chromosomes

138 revealed that *Rnf212b*$^{-/-}$ mutant spermatocytes completely failed to form foci of the crossover-

139 specific marker MLH1 (**Figure 1D**), indicating defects in the designation and/or maturation of

140 crossover-specific recombination complexes. This inference was confirmed by analyzing two

141 other crossover markers, PRR19 and CDK2 (**Figure S3**) [16, 45, 46].

142

143 **Irregular chromosome synapsis in *Rnf212b*$^{-/-}$ mutant spermatocytes**

144 To begin to understand the defects leading to crossover failure in the *Rnf212b*$^{-/-}$ mutant,

145 progression through meiotic prophase-I was assessed by quantifying the fractions of

146 spermatocytes at each substage (leptonema, zygonema, pachynema and diplonema; **Figure**

147 **1E**). Stage distributions indicated a significant overrepresentation of zygotene-stage nuclei and

148 fewer pachytene nuclei in *Rnf212b*$^{-/-}$ mutant spermatocytes relative to wild type (p = 0.001, G

149 test) suggesting delayed or unstable synapsis (**Figure 1F**). Consistently, X-Y chromosomes

150 were frequently unsynapsed in mutant spermatocytes, although they were always in close

151 proximity (**Figure 1G** and **1H**). Unsynapsed X-Y chromosomes were over 5-fold more frequent

152 in *Rnf212b*$^{-/-}$ spermatocytes relative to wild type (28.6%, n = 57/199 cells from 3 mice and 5.7%,

153 n = 9/158 cells from 3 mice, respectively; $p < 0.0001$, Fisher's exact test) and were observed

154 specifically in mid/late pachytene cells (staining positive for the histone variant H1t) indicating

155 premature X-Y de-synapsis analogous to that seen in the *Rnf212*$^{-/-}$ mutants [15].

156

157 **Intermediate steps of meiotic recombination are defective in *Rnf212b*$^{-/-}$ mutants**

158 The modest synapsis defects of the *Rnf212b*$^{-/-}$ mutant suggest that early steps of recombination

159 may occur normally, with RNF212B promoting later steps of crossover designation and/or

160 maturation. To test these inferences, a variety of recombination markers were analyzed by

161 immunostaining spermatocyte chromosome spreads (**Figures 1I**, **S4** and **S5**). RAD51 and

162 DMC1 assemble onto resected DSB ends to form nucleoprotein filaments that catalyze

163 homologous pairing and DNA strand exchange [47]. The numbers of RAD51 and DMC1 foci

164 detected in zygotene spermatocytes were slightly elevated in the *Rnf212b*$^{-/-}$ mutant relative to

165 wild type (**Figure S4**), suggesting a mild perturbation of recombination as chromosomes

166 synapse that might reflect the delayed/unstable synapsis inferred above (**Figure 1G,H**).

167

168 Replication protein A (RPA; comprising RPA1, RPA2 and RPA3) binds single-stranded DNA

169 formed at DSB ends and at D-loops as strand exchange ensues [48]. Prominent immunostaining

170 foci of RPA2 emerge in zygonema, as DMC1 and RAD51 foci are diminishing, and then

171 disappear as DSB repair ensues during pachynema. In mid-zygonema, *Rnf212b*$^{-/-}$ and wild-type

172 spermatocytes formed similar numbers of RPA2 foci, but in subsequent stages levels were

173 significantly lower in *Rnf212b*$^{-/-}$ cells suggesting that DSBs are repaired faster in the mutant

174 (**Figure S5A,B**). More dramatic reductions were observed for foci of the ZMM proteins MSH4,

175 TEX11^{Zip4} and HFM1^{Mer3}, with ~3-fold fewer foci in the *Rnf212b*$^{-/-}$ mutant (**Figures 1I,J** and **S5C-**

176 **F**). The altered dynamics of RPA2 and ZMM factors in *Rnf212b*$^{-/-}$ mutant spermatocytes were

177 similar to those seen for *Rnf212*$^{-/-}$, although reduction of MSH4 foci appears to be more severe

178 in *Rnf212b*$^{-/-}$ cells (**Figures 1I,J** and **S5**) [15].

179

180 **RNF212B dynamically localizes to synaptonemal complexes and recombination sites**

181 To address the possibility that RNF212B functions locally to stabilize ZMMs at nascent

182 crossover sites, antibodies were raised against full-length RNF212B (isoform a; **Figure S1**) and

183 used to immunostain surface-spread spermatocyte chromosomes (**Figures 2A**,**B** and **S6**).

184 RNF212B was first detected in very early zygonema, specifically localizing to sites of synapsis

185 initiation marked by SYCP1 (73.1% of short SYCP1 stretches <2 μm colocalized with RNF212B

186 foci; *n* = 38/52 from 11 nuclei). As synapsis ensued, a punctate staining pattern emerged along

187 extending SCs, with focus numbers peaking in early pachynema, just after synapsis was

188 completed, at 175.9 ± 15.2 foci per nucleus (mean ± SD; *n* = 27 nuclei; **Figure 2B**). Focus

189 numbers then diminished throughout pachynema, but at the same time a small number of large,

190 bright “amplified” RNF212B foci emerged. By late pachynema, each SC had only one or two

191 large RNF212B foci with 25.0 ± 2.3 foci per nucleus (mean ± SD; *n* = 29 nuclei; **Figure 2B**). By

192 mid-diplonema, as homologs desynapsed, all RNF212B foci had disappeared.

193

194 Super-resolution structured illumination microscopy (SIM) showed that RNF212B, like RNF212,

195 localizes specifically to the central region of the SC (**Figure 2C**). The phenotypes of *Rnf212b*$^{-/-}$

196 mutants and the localization dynamics of the RNF212B protein indicate strong similarities with

197 RNF212. To begin to explore the relationship between RNF212B and RNF212, colocalization

198 was analyzed using SIM (**Figure 2D,E**). In late zygotene/early pachytene stage spermatocytes,

199 when focus numbers peaked, an average of 307.5 ± 50.0 RNF212B foci were detected per

200 nucleus compared to 374.6 ± 43.2 RNF212 foci, and 233.4 ± 38.7 RNF212B-RNF212 co-foci.

201 Thus, RNF212-RNF212B colocalization is high but incomplete with 75.9 ± 3.4% of RNF212B

202 foci colocalized with RNF212, whereas 62.1 ± 5.1% of RNF212 foci colocalized with RNF212B

203 (means ± SDs; *n* = 11 nuclei; **Figure 2D,E**; note that many more foci are resolved by SIM than

204 by the conventional fluorescence microscopy used in **Figure 2A,B**).

205

206 SIM was also used to analyze localization of RNF212B to ongoing recombination sites marked

207 by ZMM factor MSH4 (**Figure 2F,G**). In early pachynema, RNF212B were in 2-fold excess

208 relative to MSH4 (290.0 ± 38.3 RNF212B versus 149.4 ± 17.8 MSH4 foci per nucleus; means ±

209 SDs; *n* = 7 nuclei). Reflecting this excess, only 40.2 ± 6.2 % of RNF212B foci colocalized with

210 recombination sites marked by MSH4 foci; however, 77.2 ± 4.7% MSH4 foci colocalized with

211 RNF212B (means ± SDs; *n* = 7 nuclei; **Figure 2F,G**).

212

213 In late pachynema, numbers of amplified RNF212B foci per nucleus were indistinguishable from

214 those of the crossover marker MLH1 and colocalization was essentially absolute (**Figure 2H**;

215 99.7 ± 1.0 % of RNF212B foci colocalized with MLH1 foci and 99.0 ± 1.7 % of MLH1 foci

216 colocalized with RNF212B foci; means ± SDs; *n* = 15 nuclei). Thus, RNF212B foci in late-

217 pachytene spermatocytes exclusively localize to crossover sites.

218

219 **Amplified RNF212B foci and HEI10 designate crossover sites by mid pachynema**

220 We previously showed that immunostaining foci of the ubiquitin ligase HEI10 localize to

221 designated crossover sites marked by MLH1 foci in late pachynema [16, 17]. Unlike RNF212B and

222 RNF212, we did not detect numerous HEI10 foci in zygotene and early pachytene-stage

223 spermatocytes. Instead, crossover specific HEI10 foci materialized in pachytene, similar to other

224 crossover markers such as MLH1 (**Figure 3A,B**). By sub-staging pachytene spermatocytes, we

225 showed that initial emergence of MLH1 foci occurred only in nuclei with a full complement of

226 HEI10 foci, which was already present by mid pachynema (**Figure 3A,B**), i.e. crossover

227 designation must have occurred by this stage.

228

229 Having defined HEI10 foci as the earliest detectable marker of crossover designation, we set

230 out to determine the spatial-temporal relationship with amplification of RNF212B and RNF212

231 foci. The intensity of each RNF212B or RNF212 focus was measured from images with

232 matched exposures and normalized to the mean intensities of foci in early pachytene nuclei in

233 which HEI10 foci were not yet detected (n = 2,449 RNF212B foci and 2,513 RNF212 foci; 8

234 nuclei; **Figure 3C**,**D** and **S7A**). In mid-pachytene nuclei with at least one clear HEI10 crossover

235 focus on each autosomal SC, RNF212B foci at crossover sites (i.e. colocalizing with HEI10 foci)

236 were 11-fold brighter than other RNF212B foci in the same nuclei (i.e. the average of all other

237 foci from the same 8 nuclei; 6.29 ± 2.66 for 194 crossover foci versus 0.57 ± 0.59 for 2,004

238 other foci from 8 nuclei; means ± SDs; $p < 0.0001$, Mann-Whitney test) and 6.3-fold brighter

239 than the foci detected in early pachytene nuclei, consistent with the interpretation that crossover

240 foci grow at the expense other foci. The same analysis showed that RNF212 foci located at

241 crossover sites were only 3-fold brighter than other foci in the same nuclei (1.83 ± 1.05 for 194
242 crossover foci versus 0.60 ± 0.58 for 2,291 other foci form 8 nuclei; means ± SDs; $p < 0.0001$,
243 Mann-Whitney test) and 1.8-fold brighter than those in early pachytene. Thus, at designated
244 crossover sites in mid pachytene, RNF212B foci show stronger amplification than RNF212 foci.
245
246 In late pachytene spermatocytes, the only remaining RNF212B foci were crossover specific and
247 had intensities comparable to those of the crossover foci analyzed in mid-pachytene nuclei
248 (6.42 ± 4.84-fold brighter than early pachytene foci; 206 crossover foci from 8 nuclei; mean ±
249 SD) implying that RNF212B foci do not continue to enlarge between mid and late pachytene;
250 and that RNF212B is lost from other sites as opposed to being absorbed into crossover foci. By
251 contrast, RNF212 staining in late pachytene nuclei comprised a mixture of crossover foci and
252 other small residual foci. The crossover-associated RNF212 foci in these nuclei were 6-fold
253 brighter than other foci in the same nuclei (1.53 ± 1.13 for 206 crossover foci versus 0.24 ± 0.23
254 for 988 other foci from 8 nuclei; means ± SDs; $p < 0.0001$, Mann-Whitney test) but only 1.5-fold
255 brighter than those in early pachytene. Thus, crossover-associated RNF212 foci continue to
256 differentiate between mid and late pachynema but this may occur primarily via loss of RNF212

257 from noncrossover sites as opposed to continued growth of crossover-specific foci. Consistent

258 with these inferences, the total signal intensity of RNF212B per nucleus was unchanged from

259 early to mid pachynema, but then decreased from mid to late pachynema as RNF212B was lost

260 from noncrossover sites; by comparison, total signal intensity of RNF212 reduced during both

261 early to mid, and mid to late pachynema (1.00 ± 0.21, 0.97 ± 0.24, and 0.54 ± 0.33 for

262 RNF212B; and 1.00 ± 0.32, 0.69 ± 0.31, and 0.22 ± 0.10 for RNF212 in early, mid, and late

263 pachynema, respectively, *n* = 8 nuclei each; **Figure S7C**).

264

265 Per chromosome analysis for mid-pachytene autosomes highlighted additional distinctions

266 between RNF212B and RNF212 with respect to the amplification of brighter crossover-

267 correlated foci (**Figures 3E** and **S7B**). RNF212B foci at crossover sites were on average 5.1-

268 fold brighter relative to the brightest other focus along the same chromosome, whereas RNF212

269 foci were only 1.4-fold brighter (**Figure 3E**, left). When these relative intensities were plotted for

270 individual pairs of colocalizing RNF212-RNF212B crossover foci, almost no correlation was

271 detected (r^2 = 0.106), i.e. at mid pachynema, bright RNF212B foci are not coincident with bright

272 RNF212 foci, pointing to distinct amplification behaviors of the two proteins at designated

273 crossover sites (**Figure 3E**, right).

274

275 In mid-pachynema, 76.1% of designated crossover sites (*n* = 140/184; 8 nuclei) showed

276 amplification for RNF212B foci (≥2-fold brighter relative to the brightest other focus along the

277 same chromosome) but not for RNF212 foci. Oppositely only 0.5% of crossover sites (*n* =

278 1/184; 8 nuclei) showed amplification of only RNF212 but not RNF212B (**Figure 3E**, right).

279 Together, these data imply that crossover-specific amplification of RNF212B occurs earlier than

280 that of RNF212. The distinct behaviors of RNF212B and RNF212 were most pronounced in

281 nuclei transitioning between early and mid-pachynema, as HEI10 foci were emerging (i.e. nuclei

282 with <19 HEI10 foci per nucleus; **Figure 3F**). In these nuclei, RNF212B showed clear

283 amplification at designated crossover sites but RNF212 did not.

284

285 Together, our analysis of focus dynamics in spermatocytes shows that RNF212B foci amplify at

286 designated crossover sites during early-to-mid pachytene, coincident with the appearance of

287 HEI10 foci (**Figure S8**); and then RNF212B is lost from other sites without additional

288 amplification of crossover-associated foci. By contrast, RNF212 crossover foci differentiate later,

289 during mid-to-late pachytene; and loss of RNF212 from other sites, rather than growth, may be

290 the major cause of changes in relative intensity.

291

292 **Interdependence between HEI10, RNF212B, and RNF212**

293 Our previous studies evoked a model in which RNF212 establishes a precondition for

294 crossover/noncrossover differentiation by stabilizing nascent recombination intermediates and

295 rendering further progression dependent on HEI10 [16, 17]. Notably, in *Hei10*$^{mei4/mei4}$ mutant

296 spermatocytes, abundant RNF212 foci persist along synapsed chromosomes and

297 recombination stalls at an intermediate step marked by the persistence of ZMM foci throughout

298 pachytene [16, 17]. Similarly, in early pachynema *Hei10*$^{mei4/mei4}$ mutant spermatocytes, initial

299 RNF212B staining was indistinguishable from wild type, but this pattern of abundant foci along

300 SCs persisted until early diplonema (**Figure 4A,B**). Moreover, in sharp contrast to the

301 crossover-specific pattern of amplified RNF212B foci that developed in wild-type nuclei (24.8 ±

302 2.7 foci, mean ± SD from 16 nuclei), significantly amplified RNF212B foci were not detected

303 along the majority of chromosomes in *Hei10*$^{mei4/mei4}$ mutant nuclei (**Figure 4C,D**). Specifically, for

304 54.4% of individual chromosomes from late pachytene *Hei10*$^{mei4/mei4}$ spermatocyte nuclei

305 (marked by strong H1t staining), neither the first nor the second brightest focus was ≥1.5-fold

306 brighter than the third brightest focus along the same chromosome, and only 17.0% of individual

307 chromosomes had RNF212B foci that were ≥2-fold brighter than the third brightest focus along

308 the same chromosome (*n* = 93/171 and 29/171 chromosomes, respectively; 9 nuclei; **Figure**

309 **4A,C**). The most differentiated RNF212B foci were on average only 1.6-fold brighter (with a

310 maximum of 4.2-fold) relative to the third brightest focus along the same chromosome in late

311 pachytene *Hei10*$^{mei4/mei4}$ spermatocyte nuclei; whereas in wild-type mid-pachytene nuclei,

312 RNF212B foci at crossover sites were on average 6.7-fold brighter relative to the brightest other

313 focus along the same chromosome (**Figure 4D**; 33 wild-type chromosomes with two crossover

314 foci were used for comparison to *Hei10*$^{mei4/mei4}$ chromosomes; 8 nuclei). Thus, crossover-specific

315 patterning of RNF212B appears to be largely dependent on HEI10. Reciprocally,

316 immunostaining for HEI10 in *Rnf212b*$^{-/-}$ mutant spermatocytes revealed that formation of HEI10

317 foci is dependent on RNF212B (**Figure 4E**).

318

319 Our localization analysis is incompatible with RNF212B and RNF212 functioning as an obligate

320 heterocomplex of fixed stoichiometry. Even so, immunostaining analysis in *Rnf212b*$^{-/-}$ and

321 *Rnf212*$^{-/-}$ mutants indicated an interdependent relationship. RNF212 immunostaining was

322 diminished in *Rnf212b*$^{-/-}$ mutant meiocytes and, likewise, RNF212B immunostaining was

323 diminished in *Rnf212*$^{-/-}$ cells (**Figures 4F,G** and **S9**). Immunoblotting revealed that protein levels

324 of RNF212 and, to a greater extent, RNF212B were reduced in testis extracts from *Rnf212b*$^{-/-}$

325 and *Rnf212*$^{-/-}$ mutants, respectively, relative to wild-type controls (**Figure 4H**).

326

327 Interaction between RNF212B and RNF212 was detected by yeast two-hybrid assay (Y2H), and

328 self-interaction for both proteins was also inferred, although RNF212 self-interaction appeared

329 to be much weaker than that of RNF212B (**Figure 4I,J**). Thus, RNF212B and RNF212

330 physically interact and are mutually dependent for protein stability and thus chromosomal

331 localization. Additional analysis showed that an intact RING finger domain was essential for

332 RNF212B self-interaction by Y2H, for the stability of RNF212B and RNF212 *in vivo*, and thus for

333 the pro-crossover functions of RNF212B (**Figures S10** and **S11**). Interaction between HEI10

334 and RNF212B (but not HEI10 and RNF212) was also detected, which might reflect their

335 spatiotemporal colocalization at designated crossover sites (**Figure 4I,J**).

336

337 **Similar but distinct localization of RNF212B and RNF212 in mutants defective for**

338 **recombination and synapsis**

339 The relationship between RNF212B and RNF212 was further explored by analyzing their

340 localization in mutants defective for recombination or synapsis. Repair of SPO11-induced DSBs

341 is required for the alignment and synapsis of homologs. Thus, *Spo11*$^{-/-}$ mutant meiocytes are

342 generally defective for synapsis; however, extensive stretches of SC can form between non-

343 homologous axes [49, 50]. In *Spo11*$^{-/-}$ spermatocytes, RNF212B staining was still detected

344 specifically on synapsed regions marked by SYCP1, as previously seen for RNF212 (**Figure**

345 **5A**)[15]. However, intensities of RNF212B immunofluorescence measured in *Spo11*$^{-/-}$ nuclei with

346 late zygotene/early pachytene-like morphologies (well-developed SYCP3-staining axes and

347 extensive synapsis, albeit non-homologous) were ~50% lower than those in equivalent early-

348 pachytene *Spo11*$^{+/+}$ nuclei (**Figure 5B**). By contrast, intensities of SC-associated RNF212

349 immunostaining were comparable for *Spo11*$^{-/-}$ and *Spo11*$^{+/+}$ nuclei. Correspondingly, the

350 normalized ratio of RNF212B / RNF212 immunofluorescence intensity on synapsed regions was

351 reduced by ~50% in *Spo11*$^{-/-}$ spermatocytes (**Figure 5C**). Thus, SPO11-initiated recombination

352 differentially influences the association of RNF212B and RNF212 with synaptonemal

353 complexes, with only RNF212B showing a significant dependence.

354

355 SYCP1 is the major component of the SC central region. Although *Sycp1*$^{-/-}$ mutant meiocytes fail

356 to assemble SCs, recombination initiates normally and homolog axes become coaligned [51]. In

357 *Sycp1*$^{-/-}$ spermatocytes, RNF212B staining was barely detectable in early/mid zygotene-like

358 nuclei indicating that initial association with meiotic chromosomes is strongly dependent on the

359 SC central region (**Figure S12A**). However, relatively dim RNF212B foci could be detected

360 between aligned homologous axes in late zygotene/early pachytene-like nuclei that had

361 extensive homolog coalignment (**Figures 5D**). The majority of these RNF212B foci localized to

362 recombination sites, revealed by a high level of colocalization with RPA2 (71.0 ± 8.0%; mean ±

363 S.D., *n* = 8 nuclei), as seen previously for RNF212 localization in *Sycp1*$^{-/-}$ spermatocytes

364 (**Figures 5D** and **S12B**)[15]. Thus, normal localization of RNF212B to prophase-I chromosomes is

365 strongly dependent on synapsis, with respect to both timing and abundance, but RNF212B can

366 independently localize to recombination sites, albeit inefficiently.

367

368 RNF212B focus numbers in *Sycp1*$^{-/-}$ nuclei were reduced 2.4-fold relative to *Sycp1*$^{+/+}$ controls

369 (192.1 ± 18.3 foci in *Sycp1*$^{+/+}$ versus 81.4 ± 19.3 in *Sycp1*$^{-/-}$; mean ± SDs; **Figure 5E**).

370 Correspondingly, the degree of RPA2 colocalization with RNF212B was reduced 2.4-fold (from

371 67.3 ± 3.7% in *Sycp1*$^{+/+}$ to 27.9 ± 6.0% in *Sycp1*$^{-/-}$; means ± S.D.; n = 7 and 8 nuclei,

372 respectively; p = 0.0002, Mann-Whitney test) and RNF212B-RPA2 co-foci were reduced 1.9-

373 fold (109.4 ± 7.4 foci in *Sycp1*$^{+/+}$ versus 57.9 ± 14.7 in *Sycp1*$^{-/-}$; mean ± SDs; **Figures 5F** and

374 **S12C**). In contrast, in the same nuclei, numbers of RNF212-RPA2 co-foci remained essentially

375 unchanged (122.4 ± 7.8 foci in *Sycp1*$^{+/+}$ versus 131.3 ± 17.4 in *Sycp1*$^{-/-}$; mean ± SDs) despite a

376 1.5-fold reduction in total RNF212 focus numbers (220.3 ± 13.9 foci in *Sycp1*$^{+/+}$ versus 146.9 ±

377 21.4 in *Sycp1*$^{-/-}$; mean ± SDs; **Figures 5E** and **S12C**). Moreover, the degree of RPA2-RNF212

378 colocalization was barely altered (75.2 ± 2.9% in *Sycp1*$^{+/+}$ versus 64.3 ± 11.6% in *Sycp1*$^{-/-}$; mean

379 ± SDs; p = 0.0578, Mann-Whitney test; **Figure 5F**).

380

381 We infer that the localization of RNF212B to recombination sites shows a greater dependence

382 on synapsis than does RNF212. Consequently, this differential dependency resulted in reduced

383 colocalization of RNF212B and RNF212 foci in *Sycp1*$^{-/-}$ spermatocytes (61.8 ± 9.0% of

384 RNF212B foci colocalized with RNF212, and 33.9 ± 6.3% of RNF212 foci colocalized with

385 RNF212B; versus 95.8 ± 2.4% and 83.8 ± 8.6% in *Sycp1*$^{+/+}$ nuclei; mean ± SDs; **Figure S12D**).

386

387 MLH3 and MLH1 constitute the MutLγ complex that facilitates the maturation and crossover-

388 specific resolution of double-Holliday junctions [29, 30]. Consistently, *Mlh3*$^{-/-}$ meiocytes are

389 proficient for synapsis and early steps of meiotic recombination, but defective for crossing over

390 [52]. We previously showed that MutLγ constrains HEI10 localization both temporally and spatially;

391 in *Mlh3* mutant spermatocytes HEI10 foci appear much earlier than in wild type (during

392 zygotene), are much more numerous (~90 per nucleus), and persist throughout pachytene [16]. In

393 contrast, RNF212B staining in *Mlh3*$^{-/-}$ spermatocytes was comparable to *Mlh3*$^{+/+}$ controls: focus

394 numbers peaked in early pachynema, then diminished as pachynema progressed with one or

395 two large RNF212B foci emerging on each SC (**Figures 5G**,**H** and **S12E,F**). Numbers of

396 amplified crossover-specific RNF212B foci in late pachytene *Mlh3*$^{-/-}$ nuclei were slightly lower

397 than in wild-type *Mlh3*$^{+/+}$ controls, possibly reflecting reduced stability or altered efficiency of

398 formation (**Figure S12F**). In addition, unlike wild type, some smaller foci remained on the SCs

399 until late pachynema in *Mlh3*$^{-/-}$ nuclei suggesting an additional signal following the maturation of

400 crossover sites may trigger the complete loss of RNF212B from noncrossover sites.

401 Nonetheless, this analysis indicates that the differentiation of RNF212B into crossover-specific
402 foci precedes crossing over and does not require crossover-specific factor, MutLγ. Importantly,
403 we can also infer that while crossover-specific patterning of RNF212B requires HEI10 (above,
404 **Figure 4A-D**), it does not require HEI10 *per se* to undergo crossover-specific patterning, i.e.
405 crossover-specific patterning of HEI10 appears to be downstream of initial crossover
406 designation and requires a maturation step that is dependent on MutLγ.
407
408 RNF212 staining in *Mlh3*$^{-/-}$ mutant spermatocytes was comparable to wild-type cells in early
409 pachynema, but the differentiation of crossover-specific foci was not as conspicuous; and
410 overall focus numbers remained relatively high throughout pachynema (**Figures 5G**,**I**, and
411 **S12G**). Moreover, numerous RNF212 foci persisted on synapsed regions in early diplotene
412 *Mlh3*$^{-/-}$ nuclei in which RNF212B staining was barely detectable. Together, localization studies in
413 mutant contexts extend our inference that the dynamics and regulation of RNF212B, RNF212,
414 and HEI10 are distinct.
415
416 **RNF212B is essential for crossing over in oocytes**

417 *Rnf212b*$^{-/-}$ mutation in females also caused sterility but unlike males, in which gametes were

418 absent (**Figure 1B**), the ovaries of 18 days postpartum (dpp) mice contained large numbers of

419 oocytes (**Figure 6A,B**). However, analysis of MLH1 foci in prophase-I nuclei (from fetal ovaries,

420 **Figure 6C**), and chiasmata in metaphase-I oocytes (from adult ovaries, **Figure 6D**) revealed

421 that a severe crossover defect is common to *Rnf212b*$^{-/-}$ mutants of both sexes: MLH1 foci were

422 completely absent, and chiasmata were reduced over 20-fold (1.11 ± 0.92 chiasmata per

423 nucleus in *Rnf212b*$^{-/-}$, *n* = 38 oocytes; compared to 24.6 ± 2.4 in *Rnf212b*$^{+/+}$, *n* = 28 oocytes;

424 means ± SDs).

425

426 **Sexually dimorphic chromosomal localization of RNF212B, RNF212, and HEI10**

427 RNF212B: In fetal oocytes, the initial immunostaining pattern of RNF212B during

428 zygonema was similar to that observed in spermatocytes, with foci localized specifically to

429 regions of homolog synapsis (**Figure 6E,F**). Focus numbers also peaked in early pachynema

430 (defined as pachytene-stage oocytes with ≤4 MLH1 foci from embryonic day E16.5 ovaries) but

431 were 1.6-fold greater than in spermatocytes at the same stage (**Figure 6F**; 279.0 ± 50.4 foci per

432 oocyte nucleus, *n* = 11, versus 175.9 ± 15.2 foci per spermatocyte, *n* = 27; mean ± S.D.). Also

433 distinct from spermatocytes, high numbers of RNF212B foci persisted along SCs throughout
434 pachynema both during and after the emergence of amplified foci at designated crossover sites.
435 Indeed, even after a full complement of crossover sites had matured in mid/late pachytene
436 oocytes (with ≥20 MLH1 foci, **Figure 6F**), RNF212B foci averaged 229.5 ± 45.0 per nucleus
437 (from E18.5 ovaries; mean ± SD; n = 22; **Figure 6F**). Furthermore, RNF212B remained on
438 synapsed regions throughout diplonema, as homologs desynapsed, and disappeared only as
439 oocytes entered the dictyate stage (**Figure 6E,F**).
440
441 Given the distinct dynamics of RNF212B in oocytes, we also analyzed the timing and degree of
442 amplification of RNF212B and RNF212 at crossover sites (**Figure 6G,H**). In early/mid
443 pachytene oocytes (with ≤10 MLH1 foci from E18.5 ovaries), although crossover-associated
444 RNF212B foci were on average 1.8-fold brighter than other (noncrossover) RNF212B foci in the
445 same nuclei (1.76 ± 0.58 for 28 crossover foci versus 0.98 ± 0.40 for 1,375 other foci from 7
446 nuclei; means ± SDs; $p < 0.0001$, Mann-Whitney test; **Figure 6H**), their intensity distributions
447 overlapped; indeed, we readily observed individual SCs with crossover and non-crossover
448 RNF212B foci of similar intensities (**Figure 6G**, upper panels).

449

450 By mid/late-pachynema (oocytes with ≥20 MLH1 foci from E18.5 ovaries), crossover-associated

451 RNF212B foci were now 2.5-fold brighter than other RNF212B foci, suggesting continued

452 amplification after initial designation (2.63 ± 1.13 for 250 crossover foci versus 1.07 ± 0.43 for

453 1,468 other foci from 9 nuclei; means ± SDs; $p < 0.0001$, Mann-Whitney test; **Figure 6H**). Thus,

454 in oocytes, growth/amplification of RNF212B may be coincident with crossover-site maturation

455 marked by the emergence of MLH1 foci. This contrasts spermatocytes, in which amplified

456 RNF212B foci clearly precede the appearance of MLH1 (**Figure 3**). Again, while crossover

457 associated RNF212B foci were brighter than other foci at the population level, they were not

458 always the brightest foci along the same SC (**Figure 6G**, lower panels). Moreover, a consistent

459 pattern of RNF212B foci at and surrounding designated crossover sites was not observed:

460 some crossover foci were adjacent to other similarly bright foci, others were embedded in a

461 domain of fainter foci, and others by gaps of diminished RNF212B staining (**Figure 6G**).

462 Notably, the intensities of other (noncrossover) RNF212B foci and the total signal intensity of

463 RNF212B per oocyte nucleus were largely unchanged throughout pachynema (**Figure 6H** and

464 **S13A**), in sharp contrast to the loss of RNF212B foci from non-crossover sites in spermatocytes

465 (**Figures 2, 3** and **S7**).

466 RNF212: Abundant general staining of RNF212 was also retained throughout

467 pachynema in oocytes, but amplification of RNF212 at crossover sites appeared less

468 pronounced than that of RNF212B (**Figure 6G**). Crossover-associated RNF212 foci in early/mid

469 pachynema were only 1.3-fold brighter than other foci (1.32 ± 0.47 for 30 crossover foci versus

470 0.99 ± 0.45 for 1.596 other foci from 7 nuclei; means ± SDs; $p = 0.0001$, Mann-Whitney test). By

471 mid/late pachynema, crossover-associated RNF212 were now 1.6-fold brighter than other foci in

472 the same nuclei (1.87 ± 1.04 for 245 crossover foci versus 1.19 ± 0.75 for 1,580 other foci form

473 9 nuclei; means ± SDs; $p < 0.0001$, Mann-Whitney test) and 1.9-fold brighter than those in

474 early/mid pachytene consistent with continued amplification (**Figure 6H**). Intriguingly, the

475 intensity of RNF212 at noncrossover sites slightly increased in mid/late pachynema nuclei

476 suggesting that general loading of RNF212 along SCs may continue during pachytene (0.99 ±

477 0.45 to 1.19 ± 0.75 from early/mid to mid/late pachynema; means ± SDs; $p < 0.0001$, Mann-

478 Whitney test; **Figure 6H**). Moreover, total signal intensity of RNF212 per oocyte nucleus was

479 largely unchanged between early/mid to mid/late pachynema, as seen for RNF212B (**Figure**

480 **S13A**).

481 HEI10: Chromosomal localization of HEI10 was also sexually dimorphic. Unlike
482 spermatocytes, prominent HEI10 foci were already apparent in zygotene-stage oocytes,
483 specifically at regions of synapsis (**Figure S13B**). Focus numbers increased as synapsis
484 ensued, peaking in early pachynema (defined as pachytene-stage oocytes with ≤4 MLH1 foci)
485 with 123.9 ± 28.7 foci per nucleus (mean ± SD; *n* = 18 nuclei; **Figure 7A,D**). At this stage,
486 HEI10 foci were unevenly spaced and highly variable in size and intensity; with configurations
487 suggestive of growth, shrinkage, and/or fusion of foci as might be predicted by coarsening
488 models (**Figure 7A,F** and **S13B,D**). Focus numbers then reduced as pachynema progressed,
489 showing a largely crossover-specific pattern by mid pachynema (defined as pachytene-stage
490 oocytes with ≥20 MLH1 foci from E17.5 ovaries; **Figure 7 B–E**). At this stage, 86.2 ± 9.6 % of
491 HEI10 foci colocalized with MLH1 foci and 98.0 ± 2.7 % of MLH1 foci colocalized with HEI10
492 foci (means ± SDs; *n* = 14 nuclei).
493
494 Crossover-associated HEI10 foci in early-to-mid pachynema (pachytene-stage oocytes with 5-
495 15 MLH1 foci from E16.5 ovaries) were on average 2.3-fold brighter than other foci in the same
496 nuclei (1.80 ± 0.53 for 96 crossover foci versus 0.79 ± 0.48 for 1,089 other foci from 9 nuclei;

497 means ± SDs; $p < 0.0001$, Mann-Whitney test; **Figure 7B,F**). Even very faint emergent MLH1

498 foci in early pachynema (pachytene-stage oocytes with ≤4 MLH1 foci from E16.5 ovaries)

499 tended to be associated with slightly larger HEI10 foci suggesting that amplification

500 accompanies crossover designation (1.26 ± 0.39 for 33 crossover foci versus 1.00 ± 0.45 for

501 3,817 other foci from 26 nuclei; means ± SDs; $p = 0.0003$, Mann-Whitney test; **Figure 7A,F**).

502 However, MLH1 foci emerged when HEI10 foci still outnumbered crossovers by more than 3:1,

503 i.e. before HEI10 *per se* had attained a crossover-specific distribution. Moreover, while

504 crossover-associated HEI10 foci were on average 1.9-fold brighter relative to the brightest other

505 focus along the same chromosome in early/mid pachynema (**Figure 7G**), similarly bright HEI10

506 foci were often observed along the same SC (**Figure 7B**, magnified panels, and **Figure**

507 **S13B,C**). After mid pachynema (oocytes with ≥20 MLH1 foci from E16.5 ovaries), crossover-

508 associated HEI10 foci were 3.1-fold brighter than the foci detected in early pachynema and 1.7-

509 fold brighter than the crossover-specific foci detected in early/mid pachynema (3.06 ± 1.00 for

510 186 crossover foci from 6 nuclei ; mean ± SD; **Figure 7F**), suggesting continued amplification of

511 HEI10 after crossover designation. The intensities of other remaining (noncrossover) HEI10 foci

512 in mid pachynema were comparable to those of the foci detected in early pachynema, though

513 these foci were eventually lost (**Figure 7D-F**).

514

515 Together, these data reveal profound sexual dimorphism in the localization dynamics of

516 RNF212B, RNF212, and HEI10. Importantly, in oocytes, designation of crossover sites does not

517 involve general depletion of RNF212B and RNF212 from noncrossover sites; and amplification

518 may be a coincident or downstream event. In contrast, as crossover associated HEI10 foci

519 amplify, foci at other sites progressively diminish in number. While the timing of HEI10

520 amplification may be consistent with a role in crossover-site designation, crossover sites are

521 maturing well before a crossover-specific pattern of HEI10 is attained.

522

523 **DISCUSSION**

524 **COR Patterning vis-a-vis Crossover Patterning**

525 An elementary coarsening model, that can explain crossover patterning in Arabidopsis, posits

526 that a finite amount of HEI10 protein (fixed amount per unit length) diffuses along SCs and

527 becomes progressively absorbed into one or a few amplified foci which then designate which

528 recombination sites will mature into crossovers [35, 36]. Our data in mouse are hard to reconcile

529 with this model, revealing a more complex scenario in which pattering of a given COR protein

530 may precede, accompany, or follow the designation of crossover sites; can occur with or without

531 depletion of CORs from non-crossover sites; and shows striking sexual dimorphism

532 (summarized in **Figure 7H**).

533

534 **Global and local regulation of recombination by RNF212B, RNF212, and HEI10**

535 What might be the function(s) of the observed dynamics of RNF212, RNF212B and HEI10? Our

536 analysis emphasizes the interdependencies and distinctions between the three mammalian

537 CORs and their global and local functions that help coordinate key events of meiotic prophase I.

538 Most evident is regulating the progression of recombination occurring in the context of the SC.

539 Following initial DNA strand-exchange and homolog pairing, RNF212-RNF212B associates with

540 nascent SCs and acts to stabilize ZMM factors and pause the progression of recombination. In

541 this way, RNF212-RNF212B may act to protect nascent recombination intermediates from being

542 prematurely dissociated by the Bloom complex, which is inferred to mediate the default

543 noncrossover outcome of recombination via synthesis-dependent strand annealing [31-34, 53]. This

544 early function of RNF212-RNF212B appears to promote and stabilize synapsis, possibly acting

545 as a kind of proofreading mechanism that selectively reinforces SC assembled at recombination
546 sites, i.e. between homologous chromosomes. As prophase-I progresses, connection of
547 homologs by recombinational interactions is superseded by the SC. RNF212-RNF212B could
548 mediate this hand-off by ensuring that recombinational connections are not resolved until
549 mature SC has formed.
550
551 Pausing the progression of SC-associated recombination events may also be a prerequisite for
552 crossover/noncrossover differentiation and/or to allow time for crossover sites to mature.
553 Importantly, RNF212-RNF212B renders the progression of recombination dependent on HEI10
554 (**Figure 4**) and additional pro-crossover factors including kinase CDK2, and the CNTD1-PRR19
555 complex [16, 17, 45, 54, 55]. In the absence of HEI10, foci of RNF212-RNF212B and ZMM proteins
556 remain abundant and undifferentiated along SCs, and recombination continues to be stalled
557 throughout pachytene, with DSB repair being completed only as the SC central region
558 disassembles along with RNF212-RNF212B.
559
560 At designated crossover sites, local protection of intermediates via RNF212-RNF212B may

561 enable crossover-specific events including dHJ formation and recruitment of the crossover-
562 specific resolution machinery, organized around the MutLγ endonuclease. Local stabilization of
563 SC via RNF212-RNF212B may also explain why crossover sites are the last sites to desynapse
564 during diplotene [56]. We have suggested that patches of SC retained at crossover sites may help
565 coordinate the DNA events of crossing over with exchange of the underlying chromosome axes
566 to form chiasmata.
567
568 **Distinct and interdependent functions of RNF212, RNF212B and HEI10**
569 Our ability to discern potentially distinct functions of RNF212 and RNF212B is compromised by
570 their interdependence for protein stability, i.e. *Rnf212* and *Rnf212b* single mutant phenotypes
571 likely reflect diminished function of both proteins. However, localization dynamics of RNF212
572 and RNF212B reveal divergent behaviors of the two proteins that point to distinct function and
573 regulation.
574
575 Notably, in early pachytene spermatocytes, RNF212 foci outnumber RNF212B and up to 40%
576 don't detectably colocalize. Also, the amplification of crossover specific RNF212B foci was much

577 stronger than for RNF212 and occurred earlier, with the suggestion that differentiation may
578 occur via distinct processes, e.g. redistribution to crossover sites for RNF212B, versus the loss
579 from noncrossover sites for RNF212 (or via different proportions of redistribution and loss).
580 Thus, although RNF212 and RNF212B interact, these observations argue against the existence
581 of an obligate heterocomplex of fixed stoichiometry and suggest that the activity of RNF212B
582 may be modulated by switching binding partners as it accumulates at designated crossover
583 sites. For example, RNF212B-RNF212B self-interaction could become prominent, or RNF212B
584 could partner with HEI10 in order to locally accumulate and modulate E3 ligase activities at
585 designated crossover sites. Consistent with the latter possibility, HEI10-RNF212B interaction is
586 detected by Y2H, and differentiation of RNF212B foci is both dependent on HEI10 and
587 temporally indistinguishable from its appearance at prospective crossover sites (**Figures 4** and
588 **S8**).
589
590 Localization dynamics in mutant backgrounds also point to distinct functions and regulation of
591 the three CORs. For example, RNF212 localization along SCs remains robust in the absence of
592 SPO11-catalyzed DSBs while localization of RNF212B is much less efficient, suggesting that

593 DSB signaling may stabilize RNF212B. In this respect, RNF212B may be like budding yeast

594 Zip3, which requires phosphorylation at S/T-Q consensus sites for the DNA-damage response

595 (DDR) kinases Mec1^{ATR}/Tel1^{ATM} for normal localization [57]. Further distinctions are seen in the

596 absence of synapsis, with RNF212 showing a robust ability to localize to recombination sites,

597 while RNF212B localization was much weaker. Thus, inputs from both DSBs and synapsis

598 appear to stabilize RNF212B and thereby coordinate its activity in space and time, while

599 RNF212 might act more as an anchor for localization to SCs and recombination sites. We

600 previously showed that HEI10 foci in spermatocytes are largely dependent on both DSBs and

601 synapsis [16], consistent with our inference that HEI10 foci assemble only as crossover sites

602 differentiate, dependent on RNF212-RNF212B.

603

604 Defective crossover maturation in the *Mlh3* mutant impacts the dynamics of RNF212, RNF212B

605 and HEI10 to varying degrees. Although crossover-specific patterning of RNF212-RNF212B foci

606 still occurs in *Mlh3* spermatocytes, numerous small foci of RNF212, and to a lesser extent

607 RNF212B, also persist along SCs implying that a MutLγ-dependent signal associated with the

608 maturation of crossover sites enhances the general loss of RNF212-RNF212B from

609 noncrossover sites. We previously showed that HEI10 patterning is severely perturbed in *Mlh3*

610 mutant spermatocytes, with abnormally high numbers of foci (~90 per nucleus) forming much

611 earlier than normal (in zygonema) and then persisting at recombination sites until chromosomes

612 desynapse [16]. Thus, although HEI10 is required for crossover patterning of RNF212-RNF212B

613 foci, this function does not require crossover-specific patterning of HEI10 itself, i.e. crossover-

614 specific localization of HEI10 appears to be downstream of initial crossover designation.

615 Moreover, crossover-specific patterning of HEI10 requires an upstream maturation step that is

616 dependent on the MutLγ complex, likely the dHJ formation function described by Premkumar et

617 al. [58]. Consistently, in oocytes, MLH1 foci can be detected before HEI10 foci have attained a

618 crossover-specific pattern (**Figure 7A** and **S13BC**).

619

620 Collectively, these data suggest that RNF212, RNF212B and HEI10 may function as apical

621 effectors that coordinate meiotic prophase by integrating signals from synapsis, DSB repair, cell

622 cycle kinases, and maturating crossover sites (summarized in **Figure 7**).

623

624 **Sexual dimorphism**

625 Patterning of all three CORs along SCs shows striking sexual dimorphism. In spermatocytes,
626 complete differentiation of RNF212B results in only large crossover-specific foci; while in
627 oocytes, numerous foci persist throughout pachytene even after amplified crossover-specific
628 foci have formed and crossover sites have matured (marked by the appearance of MLH1 foci;
629 **Figures 2A,H**, and **6E,G**). RNF212 dynamics are similarly dimorphic. Thus, complete
630 differentiation of RNF212B or RNF212 is not a prerequisite for the patterning and maturation of
631 crossover sites. Possibly, accumulation of a threshold level of RNF212B at a given
632 recombination site is sufficient for it to mature into a crossover. However, weak amplification and
633 incomplete differentiation in females could render RNF212B crossover foci less stable and
634 potentially reversible, possibly accounting for the inefficiency of crossover maturation
635 characterized in human oocytes that can result in unconnected (achiasmate) homologs, or
636 homologs connected only by a single telomere-proximal chiasma, configurations that are prone
637 to segregation error [8, 9]. HEI10 shows striking temporal and spatial dimorphism with foci
638 emerging in mid pachytene spermatocytes already showing a crossover distribution; while in
639 oocytes, numerous foci first form during zygotene and then attain a crossover-specific pattern in
640 pachytene.

641

642 What could account for the sexually dimorphic behavior of mammalian CORs? A pertinent

643 difference may be the duration of pachytene, which lasts almost 7 days in mouse spermatocytes

644 [59] compared to just 1-2 days in oocytes [60]. Thus, if patterning dynamics are relatively slow,

645 differentiation may remain incomplete in oocytes. Also, oocyte SCs are longer than

646 spermatocytes and CORs appear to be generally more abundant. COR dimorphism might also

647 reflect dimorphism in the DNA-damage checkpoint and gamete quality control. We previously

648 showed that RNF212 is required for oocyte quality control as dictyate oocytes assemble into

649 primordial follicles [61], while the primary checkpoint in spermatocytes occurs much earlier, as the

650 sex-body assembles in mid pachytene [62].

651

652 **FIGURES**

Ito et al., Figure 1

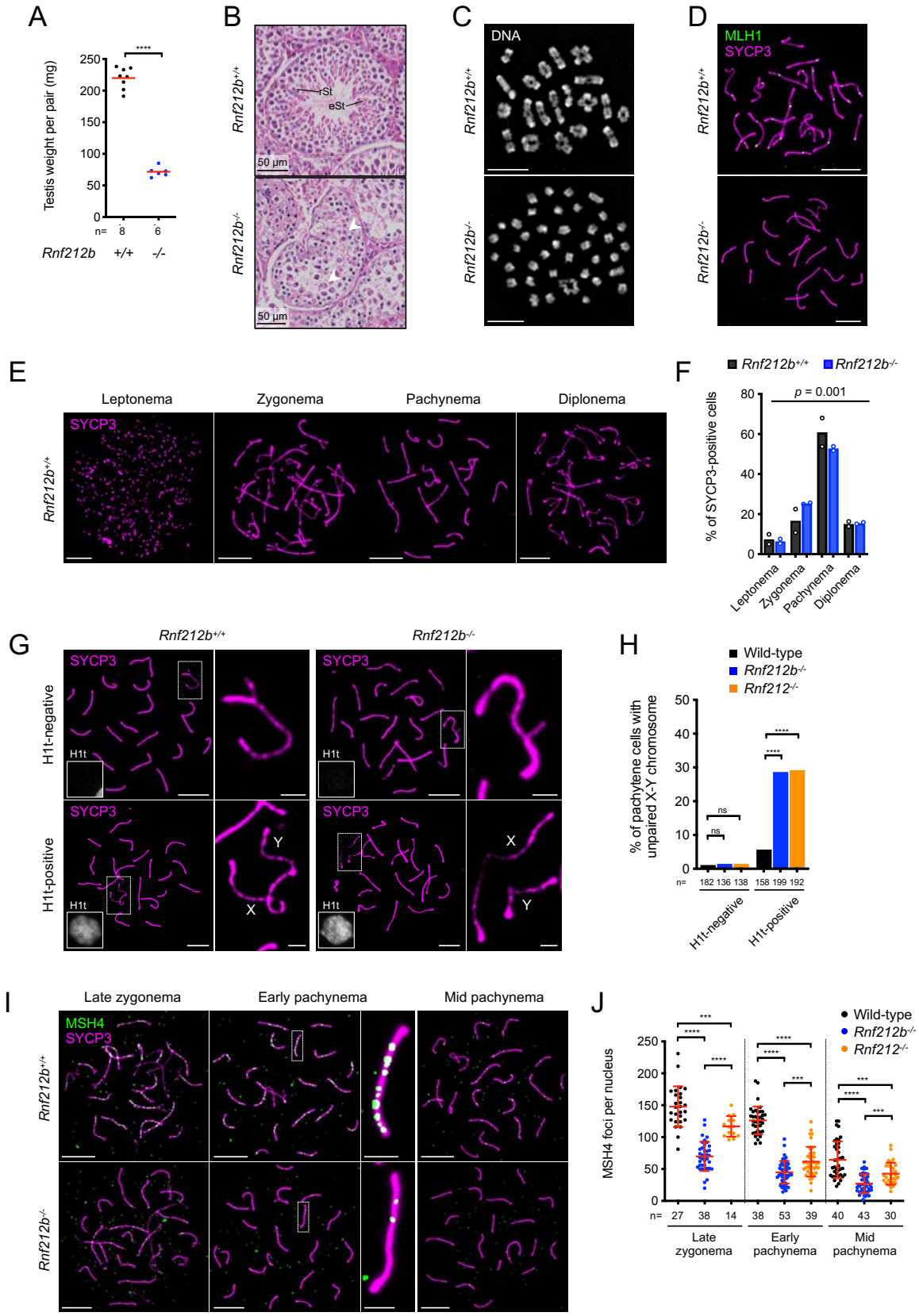

653

654 **Figure 1. RNF212B is required for crossing over via stabilization of ZMMs in mouse**

655 **spermatocytes.**

656 (A) Reduced testis size in *Rnf212b*$^{-/-}$ mutant males. Red bars indicate means. ****$p \leq 0.0001$ for

657 a two-tailed *t* test. n, numbers of mice analyzed.

658 (B) Defective spermatogenesis in *Rnf212b*$^{-/-}$ mutant males. Seminiferous tubule sections from

659 wild-type and *Rnf212b*$^{-/-}$ testes stained with hematoxylin and eosin. rSt, round spermatid; eSt,

660 elongated spermatid. Arrowheads indicate metaphase cells.

661 (C) Chiasmata are diminished in *Rnf212b*$^{-/-}$ spermatocytes. Diakinesis/metaphase-I stage

662 spermatocytes from wild-type and *Rnf212b*$^{-/-}$ testes stained with DAPI.

663 (D) MLH1 foci are absent in *Rnf212b*$^{-/-}$ spermatocytes. Mid-late pachytene-stage spermatocyte

664 nuclei from wild-type and *Rnf212b*$^{-/-}$ testes immunostained for SYCP3 and MLH1.

665 (E) Representative images of successive prophase-I stages in chromosome spreads of wild-

666 type spermatocytes immunostained for SYCP3.

667 (F) Distributions of spermatocytes in successive prophase-I stages based on SYCP3 staining.

668 >250 unselected SYCP3-positive cells were analyzed per mouse. Bar graphs indicate means of

669 two mice with plots for each mouse. $p = 0.001$ for *G* test (total cells analyzed: 578 *Rnf212b*$^{+/+}$

670 cells and 549 *Rnf212b* $^{-/-}$ cells).

671 (G) Autosomal and X-Y synapsis in wild-type and *Rnf212b*$^{-/-}$ spermatocytes. Pachytene-stage

672 spermatocyte nuclei immunostained for SYCP3 and H1t are shown. The magnified images

673 show X-Y chromosomes.

674 (H) Premature desynapsis of X-Y chromosomes in *Rnf212b*$^{-/-}$ and *Rnf212*$^{-/-}$ spermatocytes. ns,

675 not significant ($p > 0.05$); ****$p \leq 0.0001$ for Fisher's exact tests. Total numbers of cells analyzed

676 from 3 mice of each genotype are indicated below the X axis.

677 (I) Wild-type and *Rnf212b*$^{-/-}$ spermatocyte nuclei at the indicated stages immunostained for

678 SYCP3 and a ZMM factor MSH4. Representative chromosomes are magnified.

679 (J) MSH4 focus counts. Red bars indicate means ± SDs. ***$p \leq 0.001$; ****$p \leq 0.0001$ for two-

680 tailed Mann-Whitney tests. n, numbers of nuclei analyzed.

681 Scale bars, 10 μm for images of full nuclei and 2 μm for magnified panels.

682

Ito et al., Figure 2

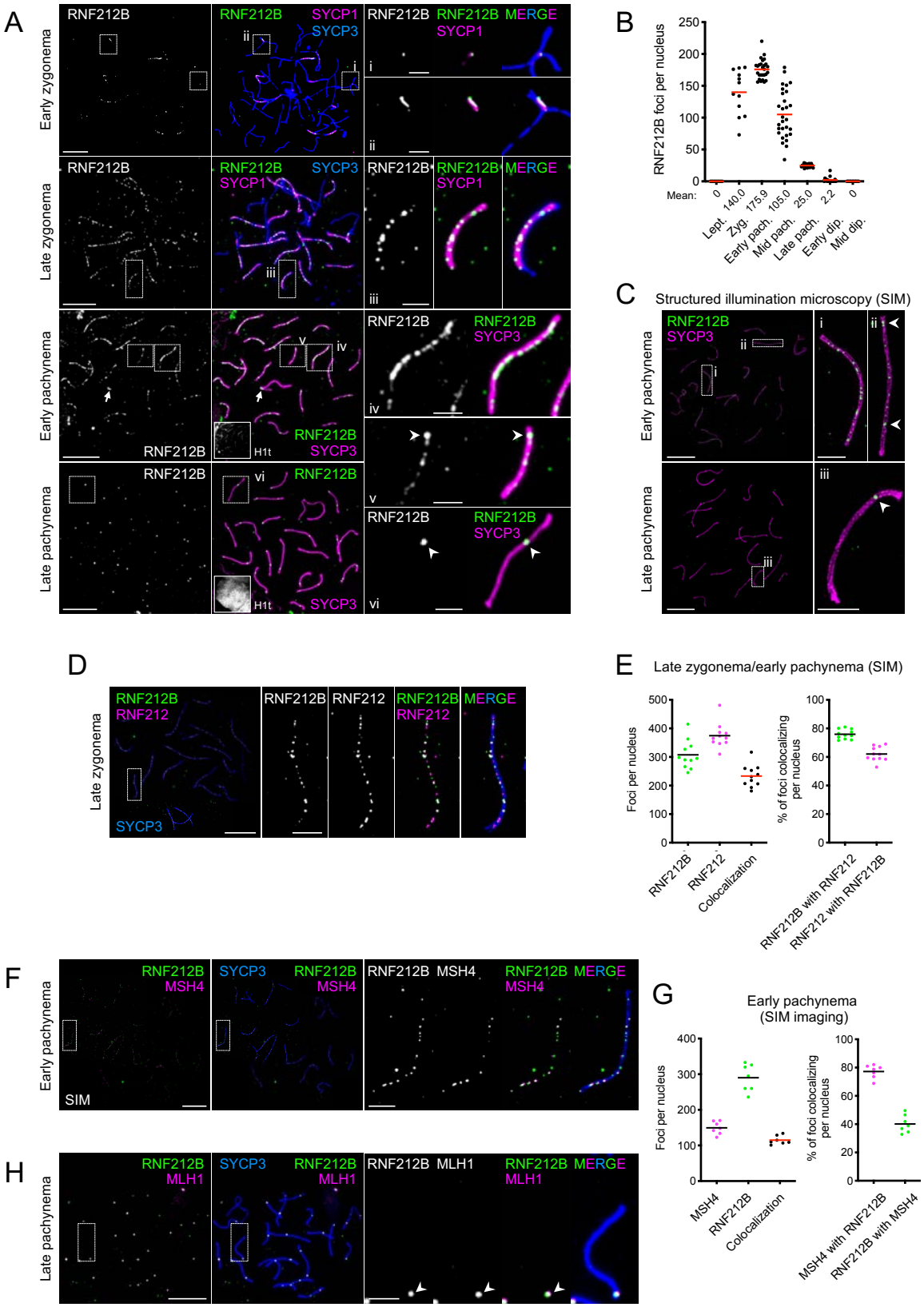

683

684 **Figure 2. RNF212B localization to synaptonemal complexes and recombination sites in**

685 **prophase I spermatocytes.**

686 (A) RNF212B localization in spermatocyte nuclei at successive prophase I stages. Images show

687 surface-spread prophase-I spermatocyte nuclei immunostained for SYCP3, SYCP1, RNF212B

688 and H1t. Arrowheads highlight large RNF212B foci. The arrow indicate synapsed pseudo-

689 autosomal region between the X-Y chromosomes.

690 (B) Numbers of RNF212B foci per nucleus in spermatocytes at successive prophase I stages.

691 Red bars indicate means. Means of focus numbers are shown below the graph. Lept.,

692 leptonema; Zyg., zygonema; pach., pachynema; dip., diplonema. Numbers of nuclei analyzed

693 were 8, 12, 27, 29, 29, 19 and 11 for in leptonema, zygonema, early pachynema, mid

694 pachynema, late pachynema, early diplonema and mid diplonema, respectively.

695 (C) RNF212B localizes to the central region of the synaptonemal complex. SIM images of early

696 and late pachytene spermatocytes immunostained for SYCP3 and RNF212B. Arrowheads

697 highlight large RNF212B foci.

698 (D) RNF212B colocalization with RNF212 in late zygonema. SIM images of a late zygotene

699 spermatocyte immunostained for SYCP3, RNF212B and RNF212.

700 (E) Quantification of RNF212B colocalization with RNF212. Left, focus counts. Right, degree of

701 colocalization. Black and red bars indicate means. 3 late-zygotene and 8 early-pachytene nuclei

702 were analyzed by SIM imaging.

703 (F) RNF212B colocalization with MSH4 in early pachynema. SIM images of an early pachytene

704 spermatocyte immunostained for SYCP3, RNF212B and MSH4.

705 (G) Quantification of RNF212B colocalization with MSH4. Left, focus counts. Right, degree of

706 colocalization. Black and red bars indicate means. 7 early pachytene nuclei were analyzed by

707 SIM imaging.

708 (H) RNF212B colocalization with MLH1. A late pachytene spermatocyte immunostained for

709 SYCP3, RNF212B and MLH1. Arrowheads indicate crossover sites.

710 Magnified images in (A), (C), (D), (F), and (H) show representative chromosomes. Scale bars,

711 10 μm for full nuclei and 2 μm for magnified images.

Ito et al., Figure 3

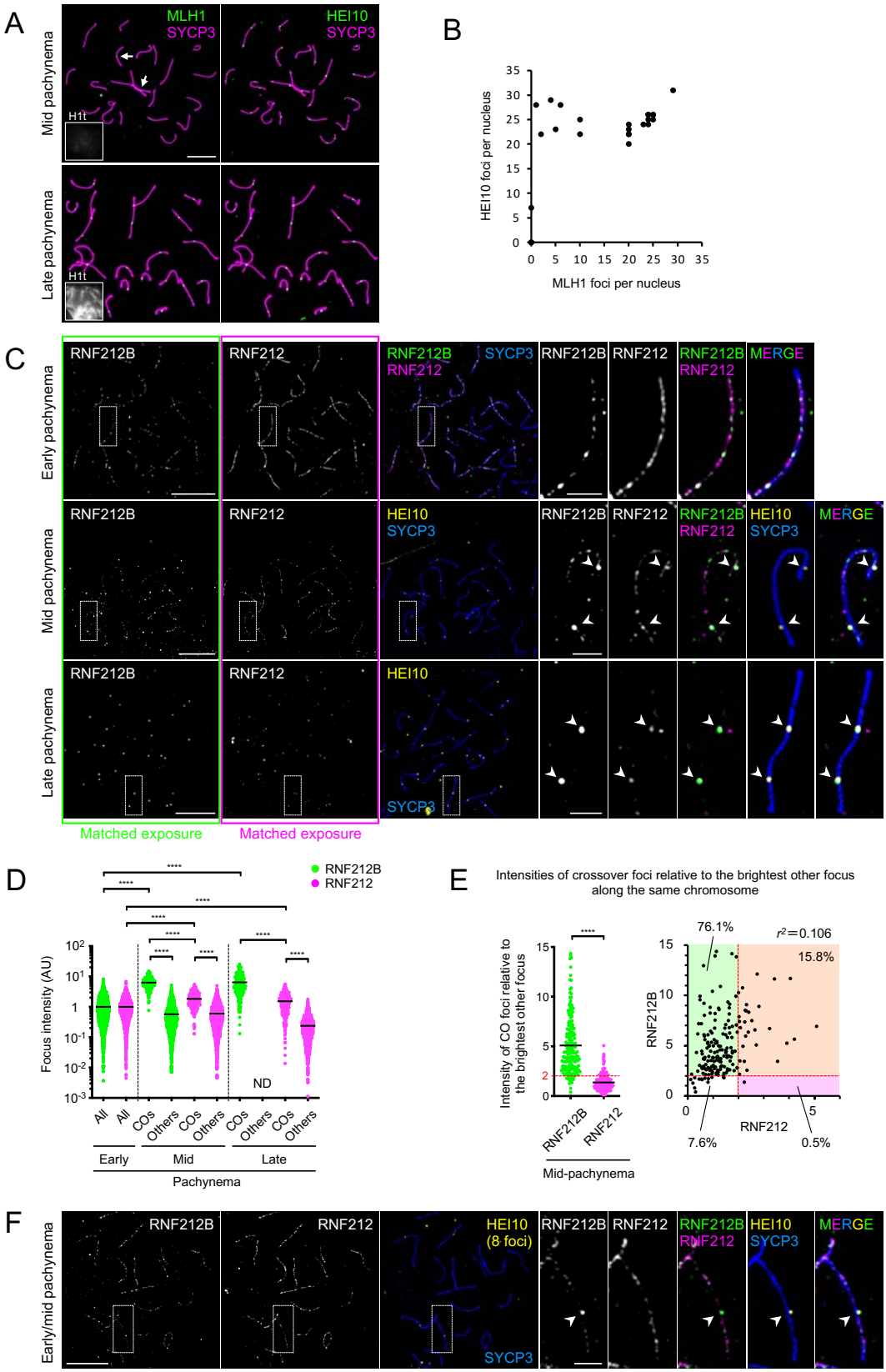

712

713 **Figure 3. Distinct timing and development of crossover-specific foci of HEI10, RNF212B**

714 **and RNF212**

715 (A) HEI10 forms crossover foci by mid-pachynema. Pachytene spermatocytes nuclei

716 immunostained for SYCP3, HEI10, MLH1 and H1t. Top images show a representative H1t-

717 negative, mid-pachytene nucleus in which small MLH1 foci are emerging on just a few

718 chromosomes (indicated by arrows) whereas bright HEI10 foci are present on all autosomes.

719 Bottom images show a representative H1t-positive late-pachytene nucleus in which both MLH1

720 and HEI10 form clear, overlapping crossover-specific foci on all autosomes.

721 (B) Quantification of HEI10 and MLH1 foci in pachytene spermatocytes confirms that MLH1 foci

722 develop only in nuclei with a full complement of HEI10 foci. 25 pachytene nuclei were randomly

723 selected and analyzed.

724 (C) Differentiation of RNF212B at prospective crossover sites is stronger than RNF212.

725 Airyscan images of early, mid and late pachytene spermatocytes nuclei immunostained for

726 SYCP3, RNF212B, RNF212 and HEI10. In all cases, RNF212B and RNF212 image exposures

727 are matched. Arrowheads indicate crossover sites marked by HEI10.

728 (D) Quantification of focus intensities for RNF212B and RNF212. Black bars indicate means.

729 ****$p \leq 0.0001$ for two-tailed Mann-Whitney tests. 8 nuclei for each stage were analyzed by

730 Airyscan imaging. Total numbers of foci analyzed: 2,449 RNF212B foci and 2,513 RNF212 foci

731 in early pachynema; 194 crossover foci, 2,004 other RNF212B foci and 2,291 other RNF212

732 foci in mid pachynema; 206 crossover foci and 988 other RNF212 foci in late pachynema. All, all

733 foci; COs, crossover foci colocalized with HEI10 foci; Others, other foci that don't colocalize with

734 HEI10 foci. ND, not detected. Quantification of focus intensities in representative individual

735 nuclei in (D) is shown in **Figure S7A**.

736 (E) Per chromosome analysis for autosomes in mid-pachytene spermatocyte nuclei. Intensity of

737 each crossover-associated RNF212B or RNF212 focus relative to that of the brightest other

738 (non-crossover) focus along the same chromosome plotted separately (left) and in two

739 dimensions (right). Red dashed lines indicate a relative focus intensity of 2. Detailed

740 representation of a per chromosome analysis is shown in **Figure S7B**. ****$p \leq 0.0001$ for two-

741 tailed Mann-Whitney tests. 186 crossover foci from 8 mid-pachytene nuclei were analyzed. Two

742 crossover-associated RNF212B foci with no other RNF212B foci along the same chromosome

743 were excluded from the plots.

744 (F) RNF212B differentiation without detectable RNF212 differentiation during early to mid

745 pachyenema. Airyscan images of an early- to mid-pachytene spermatocyte nucleus, with 8

746 HEI10 foci, immunostained for SYCP3, RNF212B, RNF212 and HEI10 are shown. Arrowheads

747 indicate crossover sites marked by HEI10.

748 Magnified images in (C) and (F) show representative chromosomes. Scale bars, 10 μm for full

749 nuclei and 2 μm for magnified images.

Ito et al., Figure 4

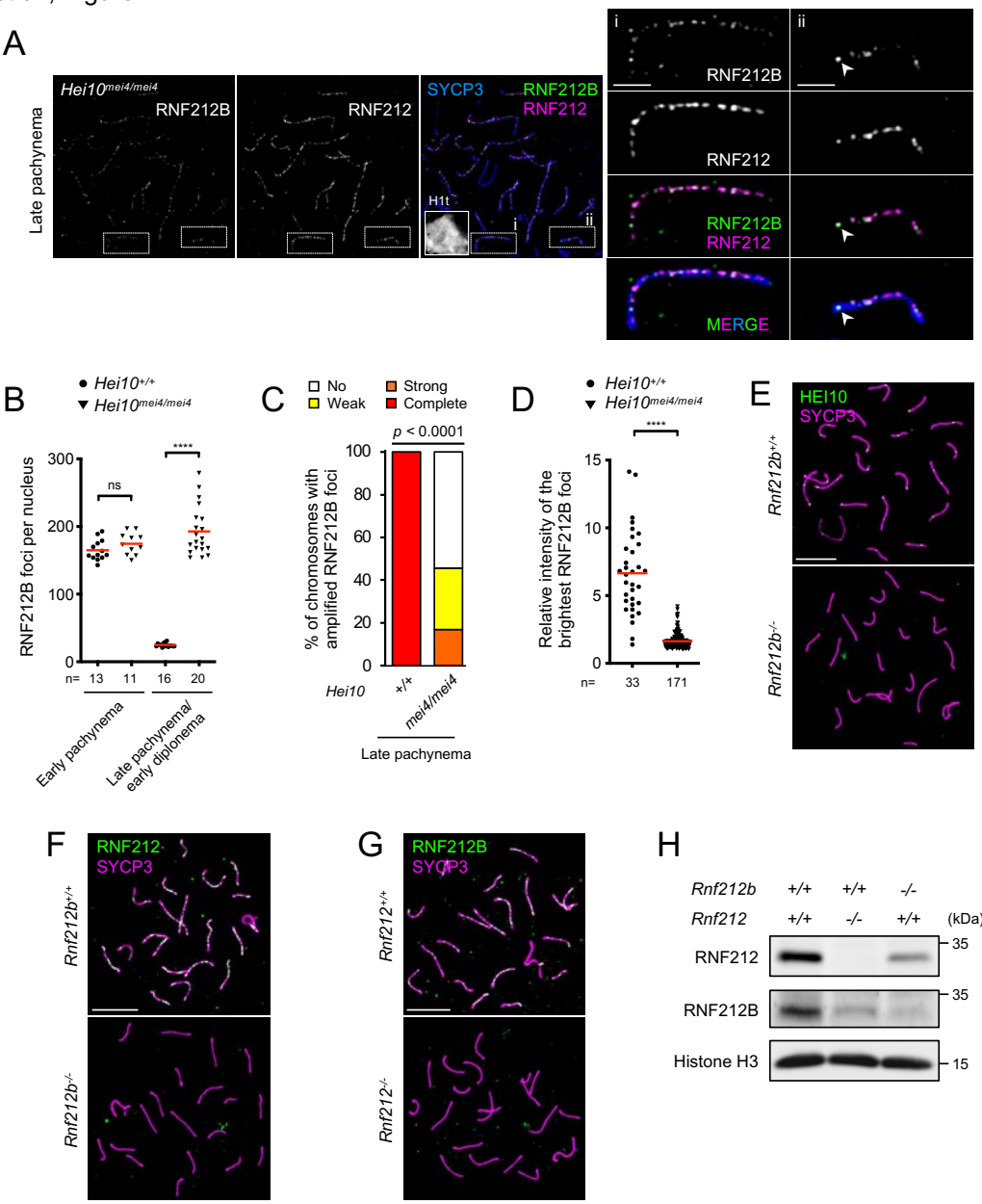

750

751 **Figure 4. Interdependent relationship between HEI10, RNF212 and RNF212B**

752 (A) Persistent RNF212B staining in *Hei10*$^{mei4/mei4}$ spermatocytes. Images of a late-pachytene

753 nucleus immunostained for SYCP3, RNF212B, RNF212 and H1t. The magnified panels show

754 representative chromosomes with: (i) no apparent differentiation of RNF212B foci; or some

755 differentiation, indicated by arrowheads. Scale bars, 10 μm in images of full nuclei and 2 μm in

756 the magnified panels.

757 (B) Focus counts of RNF212B. Red bars indicate means. Total numbers of nuclei analyzed are

758 indicated below the X-axis. For late stages, only late pachytene nuclei were analyzed for

759 *Hei10*$^{+/+}$ whereas both late pachytene and early diplotene nuclei were analyzed for *Hei10*$^{mei4/mei4}$

760 because of the early desynapsis of *Hei10*$^{mei4/mei4}$ cells [16]. ns, not significant ($p > 0.05$); ****$p \leq$

761 0.0001 for two-tailed Mann-Whitney tests.

762 (C) Differentiation of RNF212B foci. Autosomes in late-pachytene *Hei10*$^{+/+}$ and *Hei10*$^{mei4/mei4}$

763 spermatocyte nuclei were categorized into four classes based on the degree of RNF212B

764 differentiation. Strong, weak or no differentiation represents autosomes where the brightest

765 RNF212B foci were ≥2-fold, 1.5-2-fold, or <1.5-fold brighter relative to the third brightest focus

766 along the same synaptonemal complex, respectively. Complete differentiation is autosomes that

767 have only one or two bright RNF212B foci. 8 late-pachytene *Hei10*$^{+/+}$ and 9 late-pachytene

768 *Hei10*$^{mei4/mei4}$ nuclei were analyzed by Airyscan imaging. $p < 0.0001$ for a *G* test.

769 (D) Intensity of the brightest RNF212B foci relative to the third brightest focus along the same

770 chromosome in late pachytene *Hei10*$^{mei4/mei4}$ and mid pachytene *Hei10*$^{+/+}$ spermatocyte nuclei.

771 Red bars indicate means. Nuclei analyzed were the same as in (C) and **Figure 3E**, respectively,

772 but chromosomes with two crossover foci were analyzed for *Hei10*$^{+/+}$ spermatocytes. Total

773 numbers of foci analyzed are indicated below the X-axis. ****$p \leq 0.0001$ for two-tailed Mann-

774 Whitney test.

775 (E) Crossover-specific immunostaining foci of HEI10 foci were absent from chromosome

776 spreads of *Rnf212b*$^{-/-}$ spermatocytes. Mid/late pachytene nuclei from wild-type and *Rnf212b*$^{-/-}$

777 spermatocytes were immunostained for SYCP3 and HEI10. Scale bars, 10 μm.

778 (F and G) RNF212 (F) and RNF212B (G) are interdependent for chromosomal localization.

779 Early pachytene spermatocyte nuclei from the indicated genotypes were immunostained for

780 SYCP3 and RNF212 (F) or RNF212B (G). Scale bars, 10 μm.

781 (H) Interdependent protein stability of RNF212B and RNF212. Whole-testis extract from

782 indicated genotypes were subjected to immunoblotting for RNF212 and RNF212B. Histone H3

783 is a loading control.

784 (I) Yeast two-hybrid assay showing interaction between RNF212B, RNF212 and HEI10, and

785 self-interactions for RNF212B and RNF212. Yeast cells expressing Gal4 activation (Gal4-AD)

786 and binding (Gal4-BD) domain fused to the indicated proteins, or empty vectors as controls,

787 were spotted with the indicated dilutions. Aureobasidin A selection was used to detect activation

788 of the *AUR1-C* reporter. * indicates less stringent selection for *ADE2* and *HIS3* reporters.

789 (J) A summary of interactions between RNF212B, RNF212 and HEI10 detected by yeast two-

790 hybrid assays in (I).

Ito et al., Figure 5

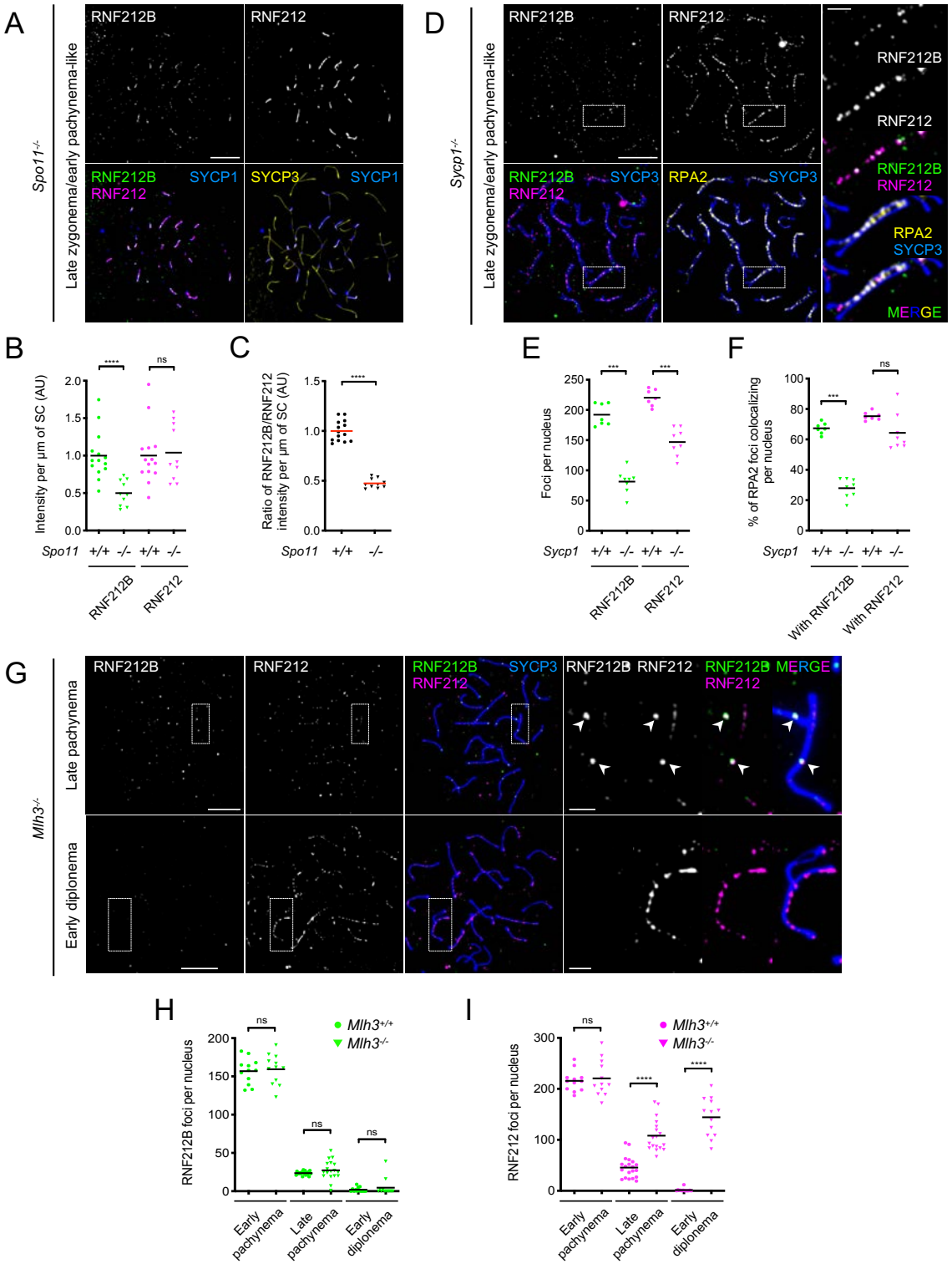

791

792 **Figure 5. Chromosomal localization of RNF212B and RNF212 in mutants defective for**

793 **recombination and synapsis**

794 (A) RNF212B and RNF212 localize to synapsed regions between non-homologous axes in

795 DSB-defective *Spo11*$^{-/-}$ spermatocytes. Images show a late zygotene/early pachytene-like

796 nucleus immunostained for SYCP3, SYCP1, RNF212B and RNF212.

797 (B and C) Staining intensities of RNF212B and RNF212 on synapsed regions. Signal intensities

798 per μm of SC per nucleus (B); and ratios of intensities per μm of SC for RNF212B relative to

799 RNF212 (C). Black and red bars indicate means. 14 early pachytene *Spo11*$^{+/+}$ nuclei and 10 late

800 zygotene/early pachytene-like *Spo11*$^{-/-}$ nuclei were analyzed.

801 (D) RNF212B and RNF212 localize to recombination sites between aligned homolog axes in

802 synapsis-defective *Sycp1*$^{-/-}$ spermatocytes. A late zygotene/early pachytene-like nucleus

803 immunostained for SYCP3, RNF212B, RNF212 and RPA2 is shown.

804 (E and F) Focus counts of RNF212B and RNF212 (E); and degree of RPA2 colocalization with

805 RNF212B and RNF212 (F). Black bars indicate means. 7 early pachytene *Sycp1*$^{+/+}$ nuclei and 8

806 late zygotene/early pachytene-like *Sycp1*$^{-/-}$ nuclei were analyzed.

807 (G) Differentiation of crossover-specific foci of RNF212B and RNF212 and persistence of

808 RNF212 staining in crossover-defective *Mlh3*$^{-/-}$ spermatocyte nuclei. Late pachytene and early

809 diplotene nuclei immunostained for SYCP3, RNF212B, and RNF212 are shown. Arrowheads

810 indicate large RNF212B foci.

811 (H and I) Numbers of RNF212B (H) and RNF212 (I) foci per nucleus in successive late

812 prophase I stages of spermatocytes. Black bars indicate means. Numbers of nuclei analyzed in

813 early pachynema, late pachynema, and early diplonema were 12, 20, and 13 for *Mlh3*$^{+/+}$; and

814 12, 18, and 13 for *Mlh3*$^{-/-}$.

815 ns, not significant ($p > 0.05$); ***$p \leq 0.001$; ****$p \leq 0.0001$ for two-tailed Mann-Whitney tests.

816 Magnified images in (D) and (G) show representative chromosomes. Scale bars, 10 μm for full

817 nuclei and 2 μm for magnified images.

Ito et al., Figure 6

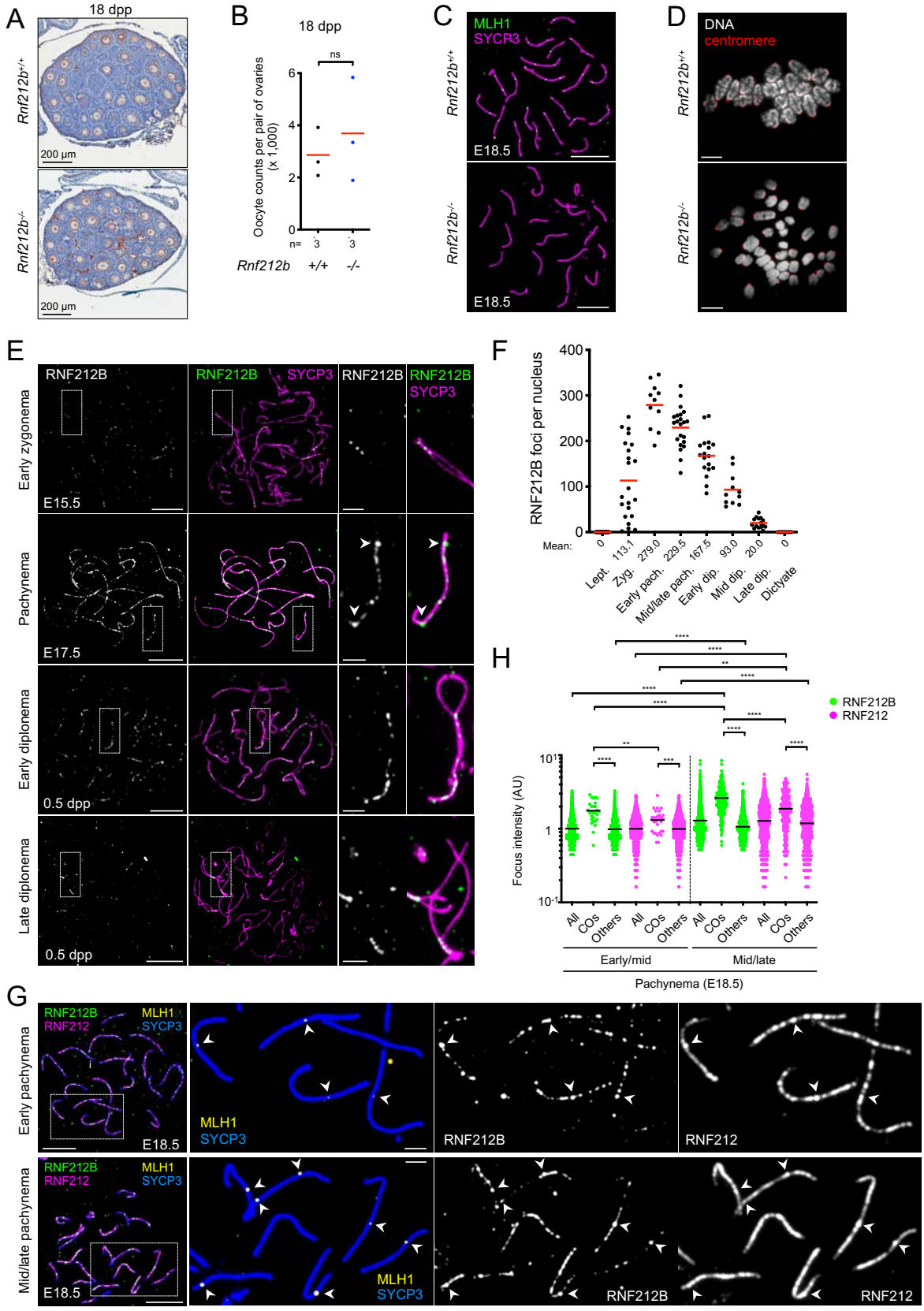

818

819 **Figure 6. RNF212B is required for crossing over and localizes to the synaptonemal**

820 **complexes and recombination sites in prophase I oocytes.**

821 (A) Ovary sections from wild-type and *Rnf212b*$^{-/-}$ mutant females at 18 days postpartum (dpp)

822 immunostained for p63 and counterstained with hematoxylin.

823 (B) Oocyte counts at 18 dpp. Red bars indicate means. ns, not significant ($p > 0.05$, two-tailed *t*

824 test). n, numbers of mice analyzed.

825 (C) MLH1 foci are absent in *Rnf212b*$^{-/-}$ oocytes. Pachytene-stage oocyte nuclei from wild-type

826 and *Rnf212b*$^{-/-}$ ovaries at embryonic day 18.5 immunostained for SYCP3 and MLH1. Scale bars,

827 10 μm.

828 (D) Chiasmata are diminished in *Rnf212b*$^{-/-}$ oocytes. Metaphase-I oocytes from ovaries of ≥2-

829 month-old wild-type and *Rnf212b*$^{-/-}$ females stained with DAPI and immunostained for CREST

830 (centromeres). Scale bars, 10 μm.

831 (E) RNF212B localization at successive prophase-I stages of fetal oocyte nuclei from embryonic

832 days 15.5 (E15.5) and 17.5 (E17.5), and 0.5 day postpartum (0.5 dpp). Surface-spread

833 prophase-I oocyte nuclei were immunostained for SYCP3 and RNF212B. Arrowheads indicate

834 large, differentiated RNF212B foci. The magnified images show representative chromosomal

835 regions. Scale bars, 10 μm for images of full nuclei and 2 μm for magnified panels.

836 (F) Numbers of RNF212B foci in oocyte nuclei at successive prophase-I stages. Red bars

837 indicate means. Means of focus numbers are indicated below the graph. Numbers of nuclei

838 analyzed in leptonema (at E15.5), zygonema (at E15.5), early pachynema (pachytene nuclei

839 with ≤4 MLH1 foci at E16.5), mid/late pachynema (pachytene nuclei with ≥20 MLH1 foci at

840 E18.5), early diplonema (at 0.5 dpp), mid diplonema (at 0.5 dpp), late diplonema (at 0.5 dpp)

841 and dictyate stage (at 0.5 dpp) are 21, 22, 11, 22, 18, 11, 15 and 7, respectively.

842 (G) RNF212B colocalization with RNF212 and MLH1 in oocytes. Early pachytene (top) and

843 mid/late pachytene (bottom) oocytes from E18.5 ovaries immunostained for SYCP3, RNF212B,

844 RNF212 and MLH1. Arrowheads indicate crossover sites. The magnified images show

845 representative chromosomal regions. Scale bars, 10 μm for images of full nuclei and 2 μm for

846 magnified panels.

847 (H) Quantification of focus intensities for RNF212B and RNF212. Black bars indicate means. ***p*

848 ≤ 0.01; ****p* ≤ 0.001; *****p* ≤ 0.0001 for two-tailed Mann-Whitney tests. 7 early/mid pachytene

849 (with ≤10 MLH1 foci) and 9 mid/late pachytene (with ≥20 MLH1 foci) nuclei from E18.5 ovaries

850 were analyzed. Total numbers of foci analyzed: 28 crossover RNF212B foci, 1,375 other

851 RNF212B foci, 30 crossover RNF212 foci and 1,596 other RNF212 foci in early/mid

852 pachynema; 250 crossover RNF212B foci, 1,468 other RNF212B foci, 245 crossover RNF212

853 foci and 1,580 other RNF212 foci. All, all foci; COs, crossover foci colocalized with MLH1 foci;

854 Others, other foci that don't colocalize with MLH1 foci.

Ito et al., Figure 7

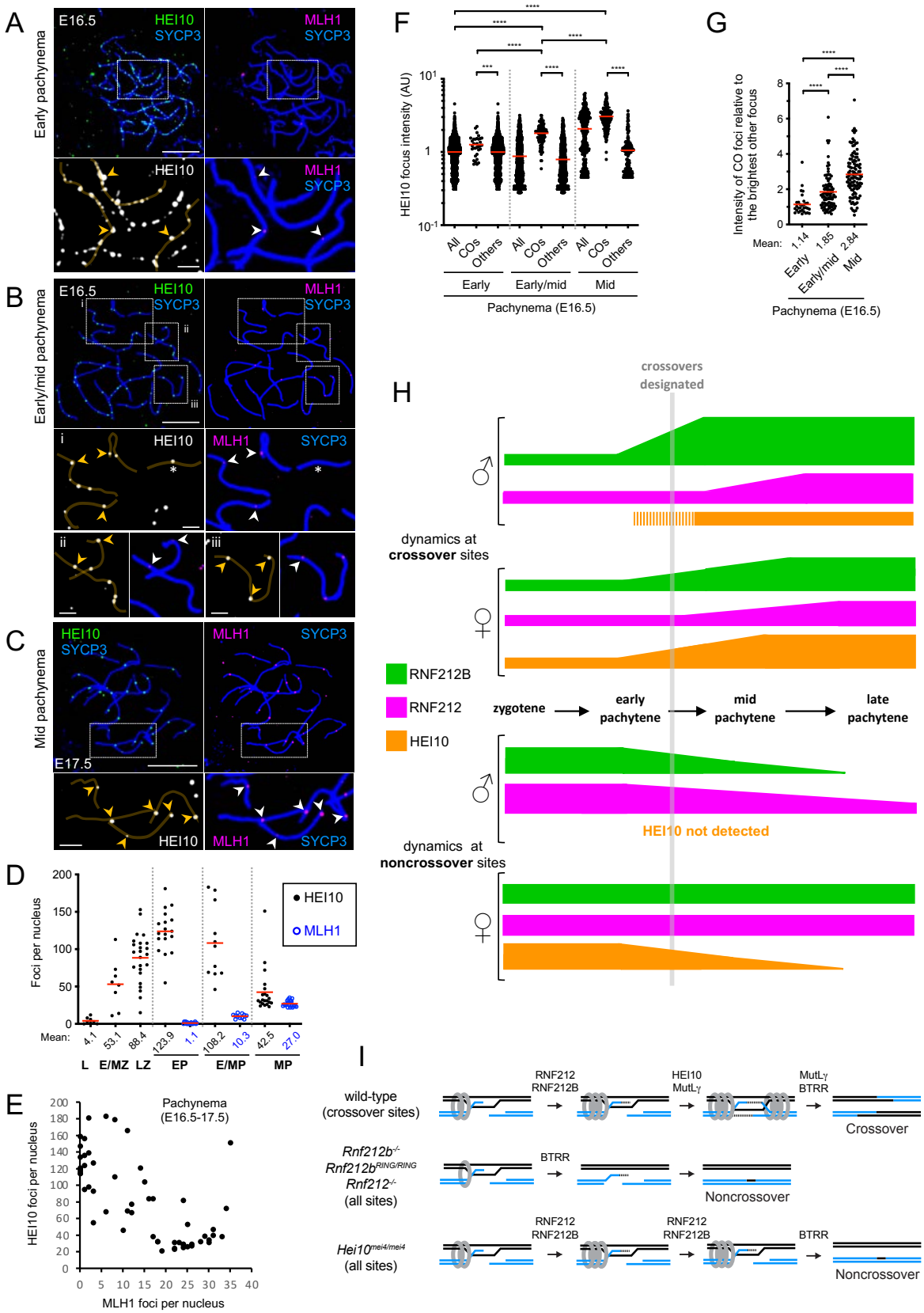

855

856 **Figure 7. Dynamic chromosomal localization of HEI10 in oocytes.**

857 (A-C) HEI10 localization at successive prophase-I stages of fetal oocyte nuclei from embryonic

858 days 16.5 (E16.5) and 17.5 (E17.5). Surface-spread prophase-I oocyte nuclei in early

859 pachynema (A), early/mid pachynema (B), and mid pachynema (C) were immunostained for

860 SYCP3, HEI10 and MLH1. Arrowheads indicate crossover foci marked by MLH1. The asterisk

861 indicates an SC with an isolated bright HEI10 focus but without an MLH focus. The magnified

862 images show representative chromosomal regions. Scale bars, 10 μm for images of full nuclei

863 and 2 μm for magnified panels.

864 (D) Numbers of HEI10 and MLH1 foci in oocyte nuclei at successive prophase-I stages. Red

865 bars indicate means. Means of focus numbers are indicated below the graph. Numbers of nuclei

866 analyzed in leptonema (L; at E16.5), early and mid zygonema (E/MZ; at E16.5), late zygonema

867 (LZ; at E16.6), early pachynema (pachytene nuclei with ≤4 MLH1 foci at E16.5), early-to-mid

868 pachynema (E/MP; pachytene nuclei with 5-15 MLH1 foci at E16.5), and mid pachynema (MP;

869 pachytene nuclei with ≥20 MLH1 foci at E16.5 and E17.5), are 8, 8, 24, 18, 11 and 21,

870 respectively.

871 (E) Quantification of HEI10 and MLH1 foci in pachytene oocytes from E16.5 and E17.5 ovaries.

872 56 pachytene nuclei were randomly selected and analyzed.

873 (F) Quantification of HEI10 focus intensities. Red bars indicate means. ***$p \leq 0.001$; ****$p \leq$

874 0.0001 for two-tailed Mann-Whitney tests. 26 early pachytene (with ≤4 MLH1 foci), 9 early/mid

875 pachytene (with 5-15 MLH1 foci) and 6 mid pachytene (with ≥20 MLH1 foci) nuclei from E16.5

876 ovaries were analyzed. Total numbers of foci analyzed: 33 crossover foci and 3,817 other foci in

877 early pachynema; 96 crossover foci and 1,089 other foci in early/mid pachynema; 186 crossover

878 foci and 180 other foci. All, all foci; COs, crossover foci colocalized with MLH1 foci; Others,

879 other foci that don't colocalize with MLH1 foci.

880 (G) Per chromosome analysis for HEI10 focus intensity. Intensity of each crossover-associated

881 HEI10 focus relative to that of the brightest other (non-crossover) focus along the same

882 chromosome. Red bars indicate means. Mean intensities are indicated below the graph.

883 Detailed representation of per chromosome analysis is shown in **Figure S13B**. ****$p \leq 0.0001$

884 for two-tailed Mann-Whitney tests. 31, 92, and 111 crossover foci from 14 early pachytene, 9

885 early/mid pachytene, and 6 mid pachytene nuclei were analyzed, respectively.

886 (H) Summary of localization dynamics of RNF212B, RNF212, and HEI10 at designated

887 crossover sites and noncrossover sites in spermatocytes and oocytes. See text for details.

888 (I) Models of crossover maturation and defects in *Rnf212b, Rnf212* and *Hei10* mutants. MutSγ

889 complexes (grey rings) bind nascent Holliday junctions and convert into sliding clamps that

890 embrace the interacting duplexes [28]. At designated crossover sites, stabilization of MutSγ (and

891 other ZMMs) by RNF212 and RNF212B stabilize single-end invasions. HEI10 and an

892 endonuclease-independent function of MutLγ[58] then facilitate second-end capture to form dHJs.

893 MutLγ-catalyzed DNA incision and the Bloom complex (BLM-TOPIIIα-RMI1-RMI2; BTRR) then

894 mediate crossover-specific dHJ resolution [29]. MutSγ is destabilized in *Rnf212b*$^{-/-}$,

895 *Rnf212b*$^{RING/RING}$ and *Rnf212*$^{-/-}$ mutants exposing nascent intermediates to unwinding by the

896 Bloom complex resulting in noncrossovers. In the *Hei10*$^{mei4/mei4}$ mutant, RNF212, RNF212B, and

897 MutSγ persist at all sites throughout pachytene, and crossover sites fail to differentiate. DSBs

898 are repaired as noncrossovers only as homologs desynapse and RNF212 and RNF212B

899 dissociate.

900

901 **SUPPLEMENTAL FIGURES**

Ito et al., Figure S1 (related to Figure 1)

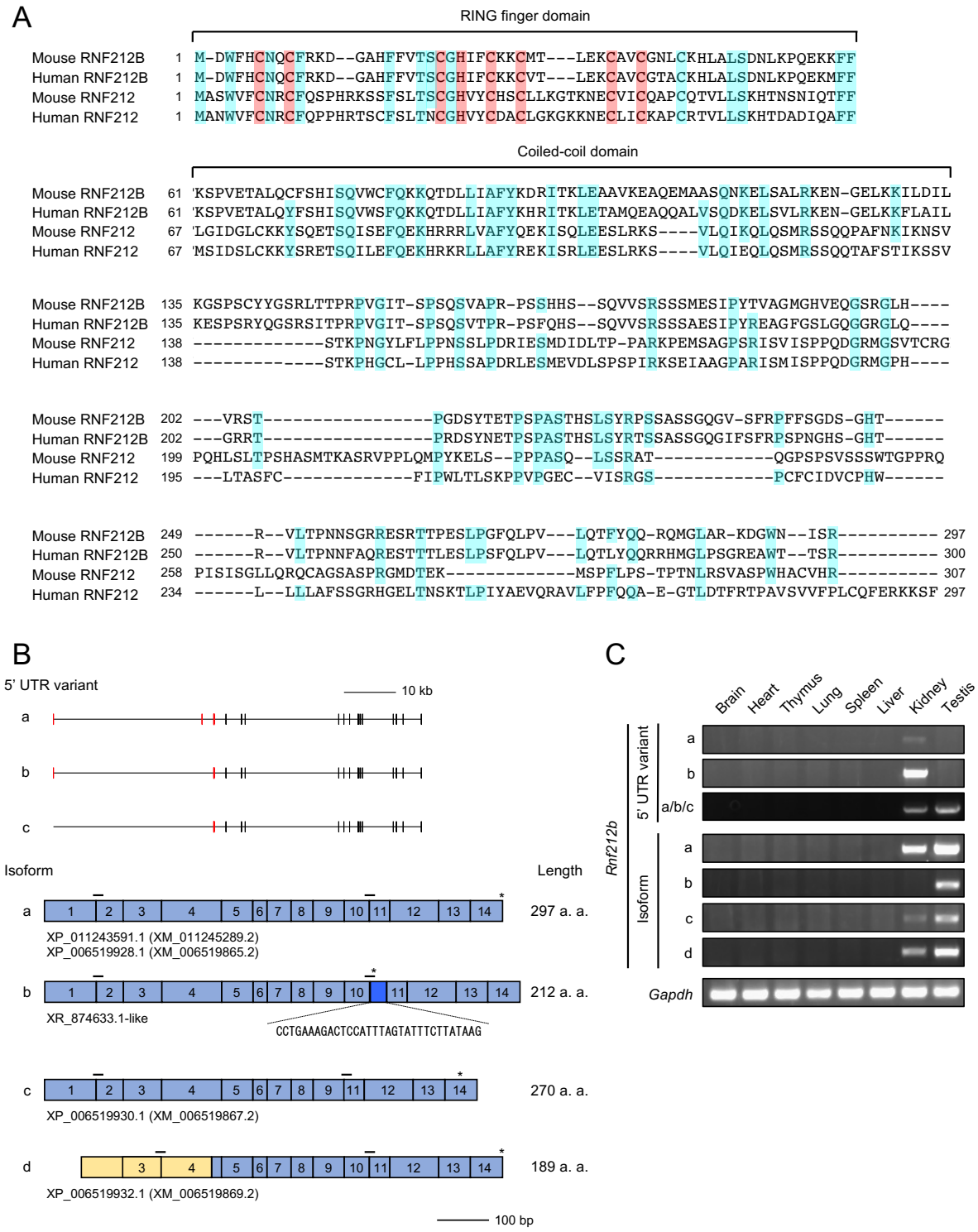

903 **Figure S1. 5' UTR variants and isoforms of mouse *Rnf212b*, related to Figure 1.**

904 (A) Protein sequence alignments of mouse and human RNF212B and RNF212 full-length

905 isoforms. Zinc-coordinating cysteine and histidine (pink) residues of RING finger domain and

906 other identical residues (blue) are highlighted.

907 (B) Schematic of 5' UTR variants and isoforms of mouse *Rnf212b*. Top, red and black bars

908 represent 5' untranslated exons (5' UTRs) and coding exons, respectively. Two 5' UTR variants

909 were identified in the NCBI database, *variants a* and *b*, which differ by a deletion of the second

910 untranslated exon in *variant b*. A third *variant c* was identified by 5' RACE from testes and

911 comprises ~1/3 of the third untranslated exon of *variant a* followed by the 14 coding exons.

912 Bottom, yellow and blue boxes represent 5' UTRs and coding exons, respectively. Four different

913 coding isoforms were identified in the NCBI database. For simplicity, 5' UTRs of isoforms a-c are

914 not shown. Isoform a encodes the full-length RNF212B protein of 297 amino acids; isoform b

915 uses an alternative splice acceptor site, creating a premature stop codon after exon 10 that is

916 predicted to produce a protein lacking 86 C-terminal amino acids; isoform c uses an alternative

917 splice donor site to precisely skip exon 10, which corresponds to 16 amino acids of the

918 disordered serine-rich C-terminal tail, resulting in a predicted protein of 270 amino acids; and

919 isoform d lacks the first two exons present in other isoforms and uses an extended exon 3 and

920 most of exon 4 as a 5' UTR, to encode a predicted protein of 189 amino acids that lacks the N-

921 terminal RING finger domain. Asterisks indicate positions of stop codons. Horizontal bars

922 represent positions of primers used to detect each isoform by RT-PCR in (C). Annotated or

923 related variants and isoforms in the NCBI database are also shown. Expression of full-length a

924 and b isoforms in testis was confirmed by *de novo* cloning from testis mRNA (the sequence of

925 cloned isoform b was similar but not identical to XR_874633).

926 (C) Expression of mouse *Rnf212b* 5' UTR variants and isoforms analyzed by RT-PCR. Total

927 RNA was extracted from indicated tissues of mature male mice and subjected to RT-PCR.

928 *Gapdh* is a loading control.

Ito et al., Figure S2 (related to Figure 1)

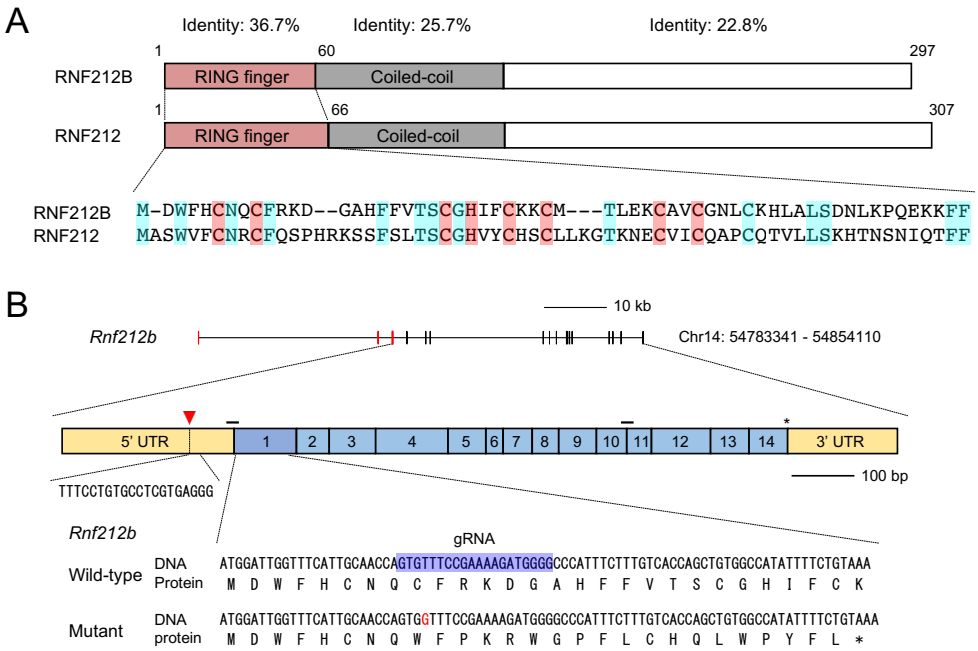

Figure S2. Domain structure of RNF212B and strategy to generate *Rnf212b* mutant mice by CRISPR/Cas9, related to Figure 1.

(A) Domain structures of mouse RNF212B and RNF212. Amino acid sequences of the RING finger domains are shown below. Presumptive zinc-coordinating cysteines and histidines and other identical residues are highlighted in pink and blue, respectively. The domain structure of the full-length RNF212B protein mirrors that of RNF212 with an N-terminal RING finger domain (36.7% amino-acid identity with RNF212), a ~70 amino acid region of predicted coiled-coil (25.7% identical) and a largely disordered serine-rich C-terminal tail (22.8% identical).

(B) Schematic of the mouse *Rnf212b* gene on chromosome 14. Top row: red and black bars

939 represent 5’ untranslated exons (5’ UTRs) and coding exons, respectively. Middle row: yellow

940 and blue boxes represent 5’ UTRs and coding exons, respectively, in the full-length isoform a.

941 The inverted red triangle represents the translation initiation site in testis identified by 5’ RACE.

942 An asterisk represents the stop codon. Horizontal bars represent the positions of primers used

943 to detect 5’ UTR variants a/b/c by RT-PCR in **Figure S1C**. Bottom row: nucleotide and amino-

944 acid sequences at the CRISPR/Cas9 targeted site in exon 1. A single-nucleotide insertion

945 (shown in red) created a frameshift and premature stop codon (asterisk). The guide RNA

946 (gRNA) sequence is highlighted in blue.

947

Ito et al., Figure S3 (related to Figure 1)

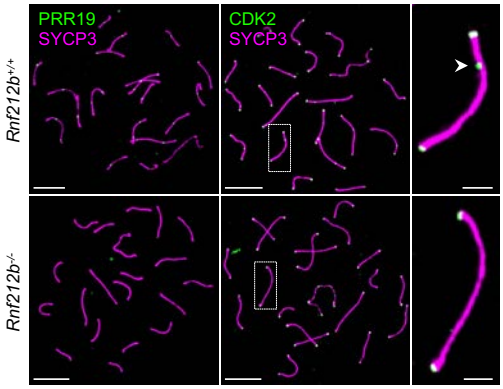

948

949 **Figure S3. Absence of crossover markers in *Rnf212b*$^{-/-}$ mutant mice, related to Figure 1.**

950 Crossover-specific immunostaining foci of PRR19 (left) and CDK2 (right) foci were absent from

951 chromosome spreads of *Rnf212b*$^{-/-}$ spermatocytes. Mid/late pachytene nuclei from wild-type and

952 *Rnf212b*$^{-/-}$ spermatocytes were immunostained for SYCP3 plus PRR19 (left) or CDK2 (right).

953 The magnified images show representative chromosomes from the CDK2 staining. Note that

954 CDK2 also localizes to telomeres, which is not affected by *Rnf212b* mutation. An arrowhead

955 indicates an interstitial CDK2 focus marking a prospective crossover site. Scale bars, 10 μm for

956 images of full nuclei and 2 μm for magnified panels.

Ito et al., Figure S4 (related to Figure 1)

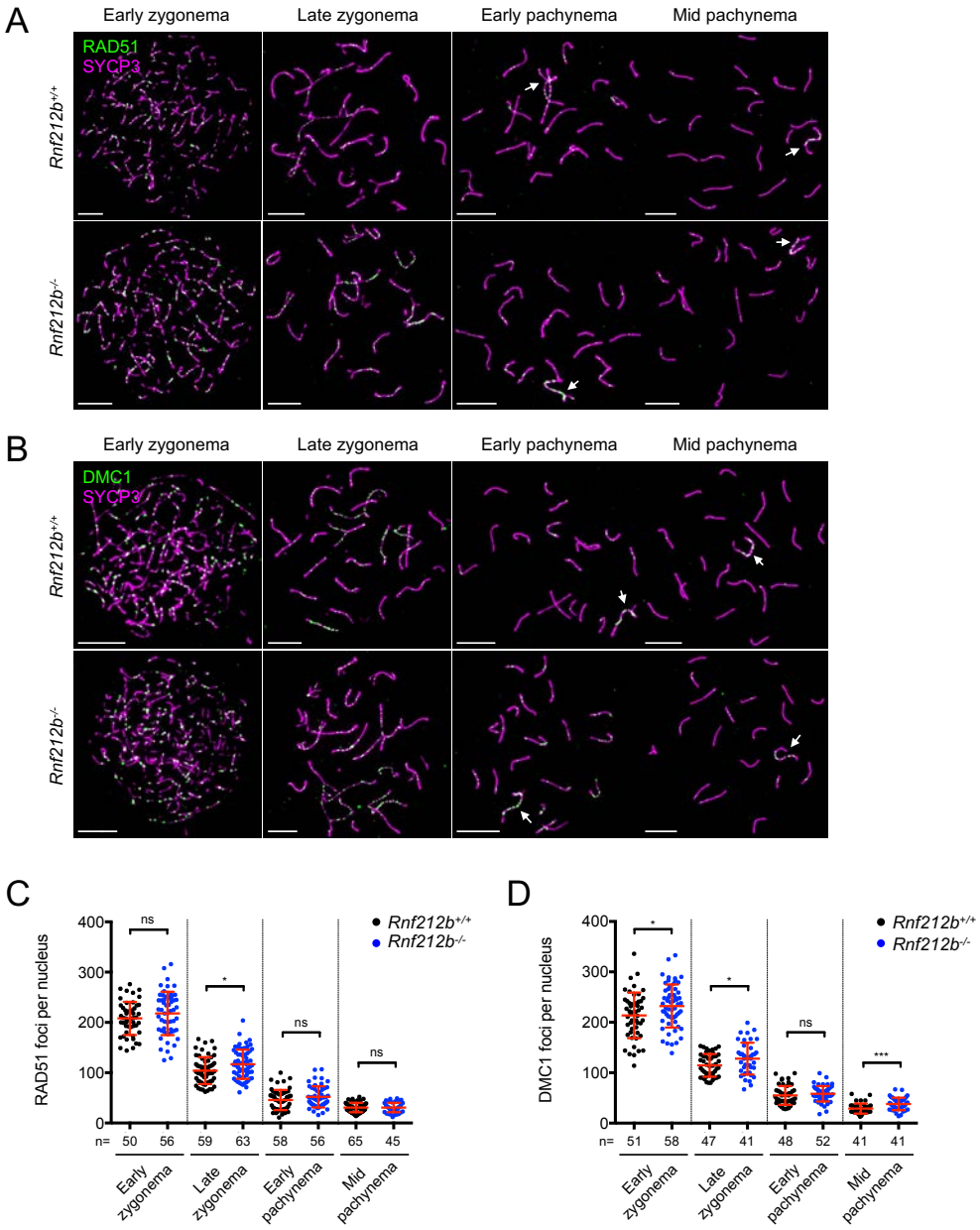

957

958 **Figure S4. Dynamics of RAD51 and DMC1 throughout zygonema and pachynema, related**

959 **to Figure 1.**

960 (A and B) Representative images of RAD51 (A) and DMC1 (B) immunostainings in wild-type

961 and *Rnf212b*$^{-/-}$ spermatocytes nuclei immunostained for SYCP3 plus RAD51 (A) or DMC1 (B) at

962 the indicated stages. Arrows indicate the X-Y chromosomes. Scale bars, 10 μm.

963 (C and D) Focus counts of RAD51 (C) and DMC1 (D). Red bars indicate means ± SDs.

964 ns, not significant ($p > 0.05$); *$p \leq 0.05$; ***$p \leq 0.001$ for two-tailed Mann-Whitney tests. Total

965 numbers of nuclei analyzed are indicated below the X axes.

Ito et al., Figure S5 (related to Figure 1)

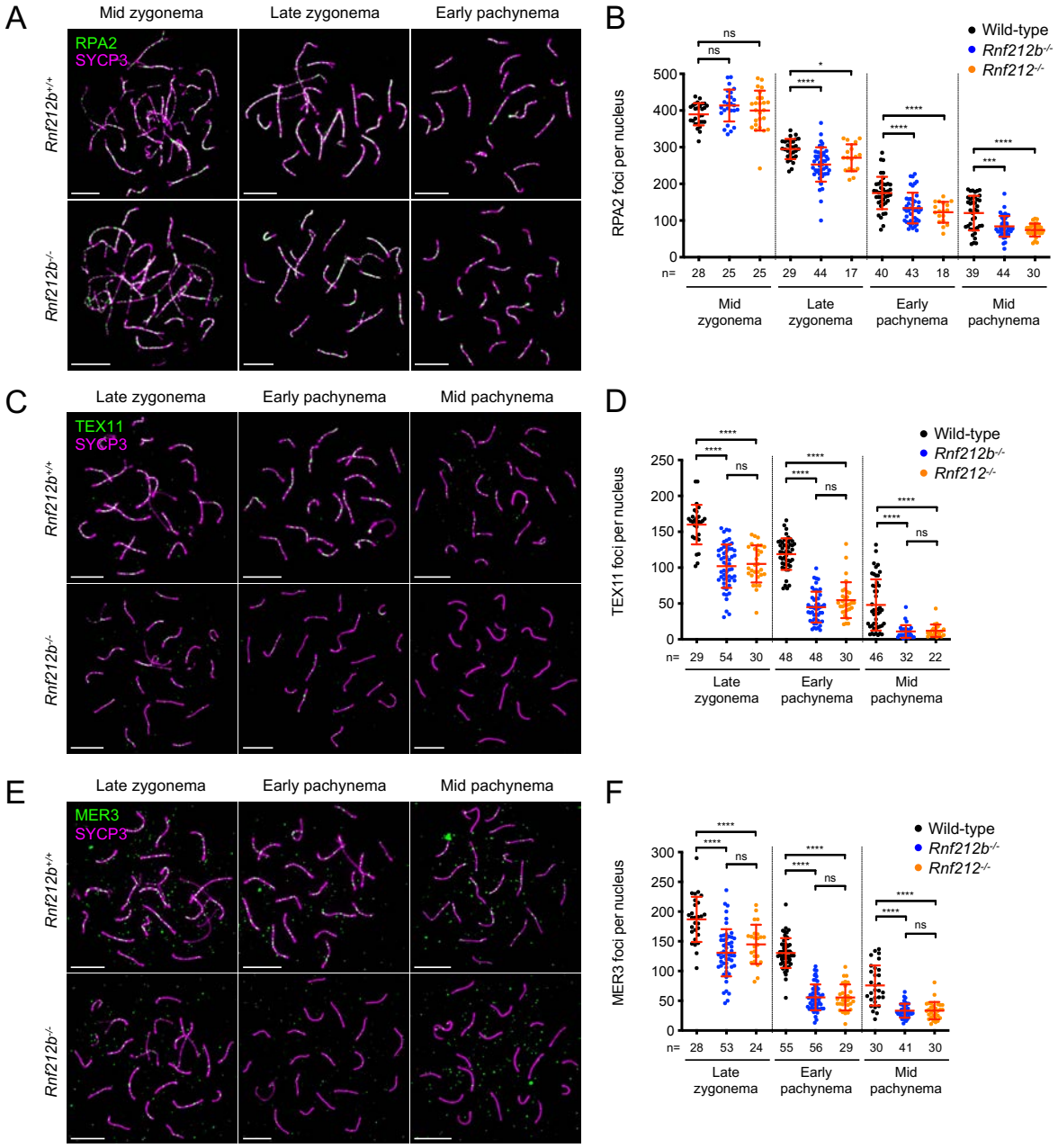

966

967 **Figure S5. Intermediate steps of recombination are perturbed in *Rnf212b*$^{-/-}$ mutant mice,**

968 **related to Figure 1.**

969 (A, C and E) Images of wild-type and *Rnf212b*$^{-/-}$ spermatocyte nuclei immunostained for SYCP3

970 plus RPA2 (A), TEX11 (C) or MER3 (E) at the indicated stages. Scale bars, 10 μm.

971 (B, D and F) Counts of RPA2 (B), TEX11 (D) and MER3 (F) immunostaining foci. Red bars

972 indicate means ± SDs. ns, not significant ($p > 0.05$); *$p \leq 0.05$; ***$p \leq 0.001$; ****$p \leq 0.0001$ for

973 two-tailed Mann-Whitney tests. Total numbers of nuclei analyzed are indicated below the X

974 axes.

Ito et al., Figure S6 (related to Figure 2)

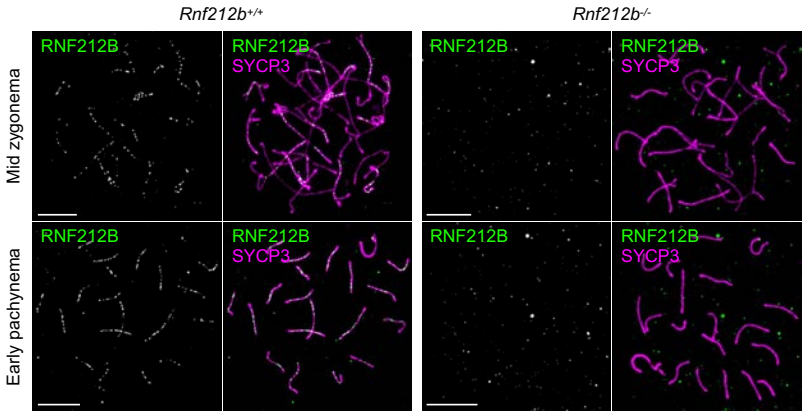

975

976 **Figure S6. Specificity of anti-RNF212B antibody, related to Figure 2.**

977 Wild-type and *Rnf212b*$^{-/-}$ spermatocyte nuclei at indicated stages were immunostained for

978 SYCP3 and RNF212B. Scale bars, 10 μm.

Ito et al., Figure S7 (related to Figure 3)

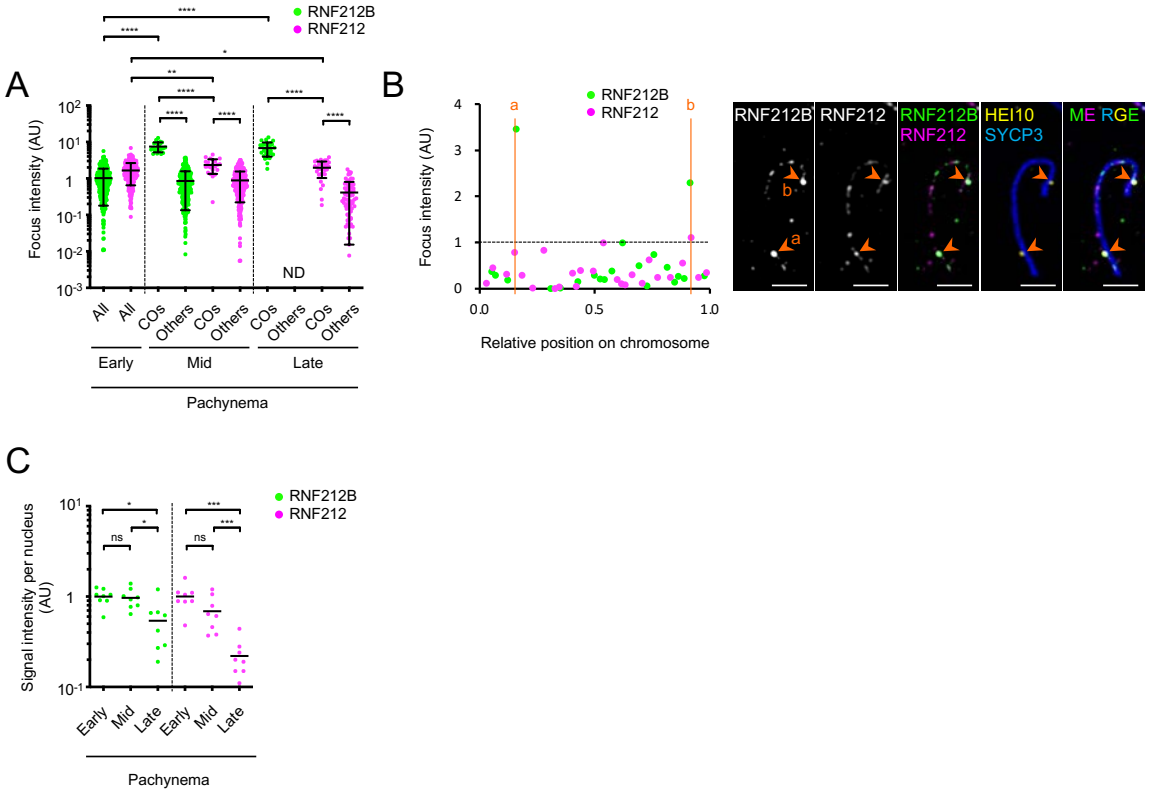

Figure S7. Distinct localization dynamics of RNF212B and RNF212 foci, related to Figure 3.

(A) Quantification of focus intensities for RNF212B and RNF212. Each dot represents each focus of RNF212B and RNF212 from the early, mid and late pachytene nuclei (one nucleus per stage) analyzed in **Figure 3D**. Bars indicate means ± SDs. All, all foci; COs, crossover-specific foci that colocalize with HEI10 foci; Others, foci that don't colocalize with HEI10 foci (noncrossover foci). ND, not detected. *$p \leq 0.05$; **$p \leq 0.01$; ****$p \leq 0.0001$ for two-tailed Mann-Whitney tests.

988 (B) Representation of per chromosome analysis of RNF212B and RNF212 foci for a mid-

989 pachytene chromosome (shown in the images in the right-hand panels). Each focus of

990 RNF212B or RNF212 is represented by a dot. The dashed line indicates the signal intensity of

991 the brightest other focus (noncrossover focus) along the same chromosome. Orange vertical

992 lines indicate the positions of HEI10-positive crossover sites (a) and (b). Intensities of foci at

993 these sites relative to that of the brightest other (noncrossover) focus are: (a) 3.5 and (b) 2.3 for

994 RNF212B; and (a) 0.8 and (b) 1.1 for RNF212.

995 (C) Total signal intensity of RNF212B and RNF212 per nucleus in early, mid and late pachytene

996 spermatocytes. Black bars indicate means. ns, not significant ($p > 0.05$); *$p \leq 0.05$; ***$p \leq 0.001$

997 for two-tailed Mann-Whitney tests. Nuclei analyzed were the same as in **Figure 3D**.

Ito et al., Figure S8 (related to Figure 3)

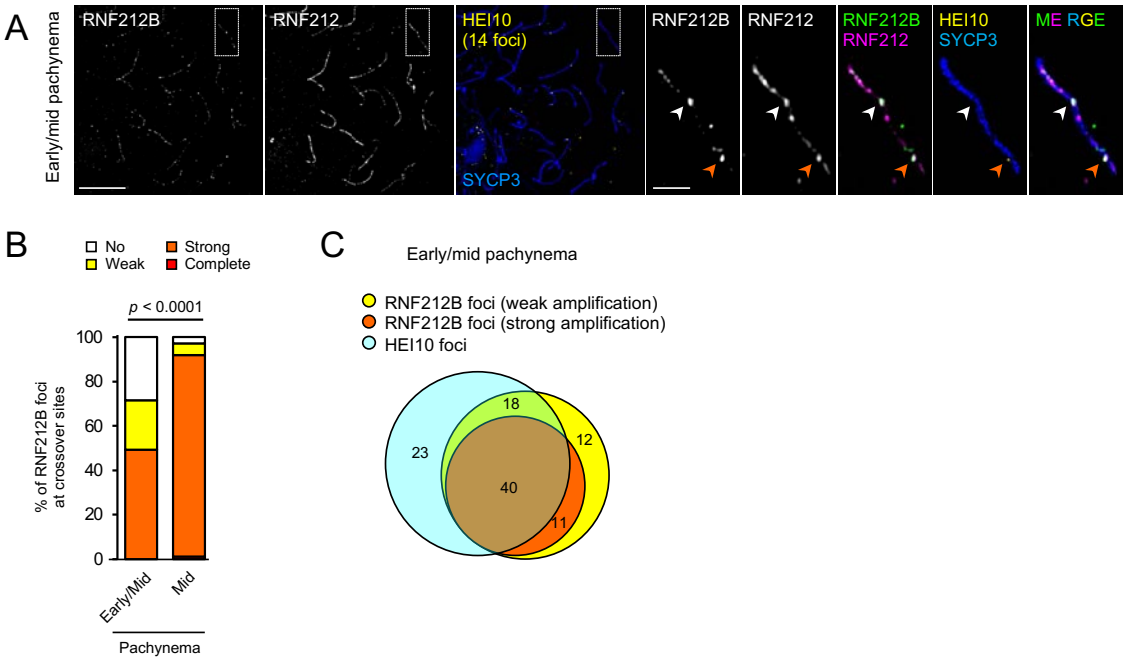

Figure S8. Timing of RNF212B focus amplification and appearance of HEI10 foci in spermatocytes, related to Figure 3.

(A) Amplification of RNF212B foci relative to the emergence of HEI10 foci. Airyscan images of an early-to-mid pachytene spermatocyte nucleus immunostained for SYCP3, RNF212B, RNF212 and HEI10. This nucleus contains 14 HEI10 foci indicating that it is in transition to a full complement of designated crossovers sites (≥20 HEI10 foci). The white arrowhead indicates an amplified RNF212B focus without an associated HEI10 focus; and the orange arrowhead indicates an amplified RNF212B focus colocalized with a small, emerging HEI10 focus. These configurations indicate that growth of RNF212B foci can precede a detectable HEI10 focus.

1008 (B) Amplification of RNF212B at crossover sites. Crossover-specific foci of RNF212B (i.e.

1009 RNF212B foci that colocalized with HEI10 foci) in early-to-mid pachytene nuclei (containing 5-18

1010 HEI10 foci), and mid-pachytene nuclei (≥19 HEI10 foci) were classified based on their degree of

1011 amplification by measuring their intensity relative to the brightest other (noncrossover)

1012 RNF212B focus along the same chromosome (complete means no other foci detected along the

1013 SC; strong, ≥2-fold brighter; weak, 1.5-2-fold brighter; or no amplification, <1.5-fold brighter). 81

1014 crossover-specific RNF212B foci from 7 early-to-mid pachytene and 186 crossover-specific

1015 RNF212B foci from 8 mid-pachytene nuclei were analyzed by Airyscan imaging. In early-mid

1016 pachytene nuclei, the majority of HEI10 foci are associated with detectable amplification of

1017 RNF212B but 28% are not.

1018 (C) Amplification of RNF212B and emergence of HEI10 foci in early-to-mid pachynema.

1019 Numbers of HEI10 foci (sky blue), and RNF212B foci with weak (yellow) and strong

1020 amplification (orange) are shown. Criteria for RNF212B focus amplification are as in (B). 71.6%

1021 (58/81 foci) of sites marked by HEI10 were coincident with weak or strong amplification of

1022 RNF212B, while 78.4% (40/51 foci) of strongly amplified RNF212B foci colocalized with a HEI10

1023 focus. Thus, with respect to the amplification of RNF212B and the emergence of HEI10 at

1024 prospective crossover sites, a sequential order of events is hard to discern, i.e. these events

1025 may be coincident, consistent with the dependence of RNF212B focus differentiation on HEI10.

1026 7 early-to-mid pachytene nuclei with 5-18 HEI10 foci per nucleus were analyzed by Airyscan

1027 imaging.

1028

Ito et al., Figure S9 (related to Figure 4)

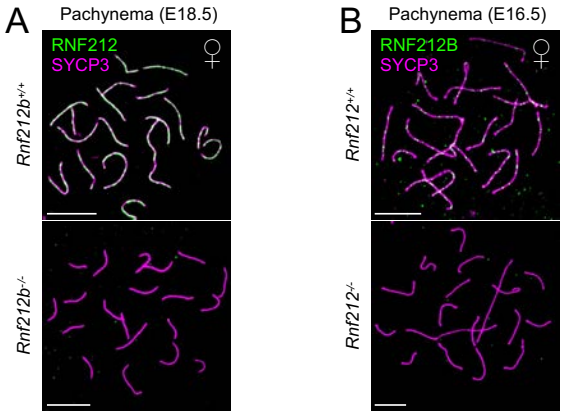

1029

1030 **Figure S9. Interdependent chromosomal localization of RNF212B and RNF212 in oocytes,**

1031 **related to Figure 4.**

1032 (A and B) RNF212 (A) and RNF212B (B) are interdependent for chromosomal localization.

1033 Pachytene-stage oocytes at embryonic day 18.5 or 16.5 (E18.5 or E16.5) from the indicated

1034 genotypes were immunostained for SYCP3 and RNF212 (A) or RNF212B (B). Scale bars, 10

1035 μm.

Ito et al., Figure S10 (related to Figure 4)

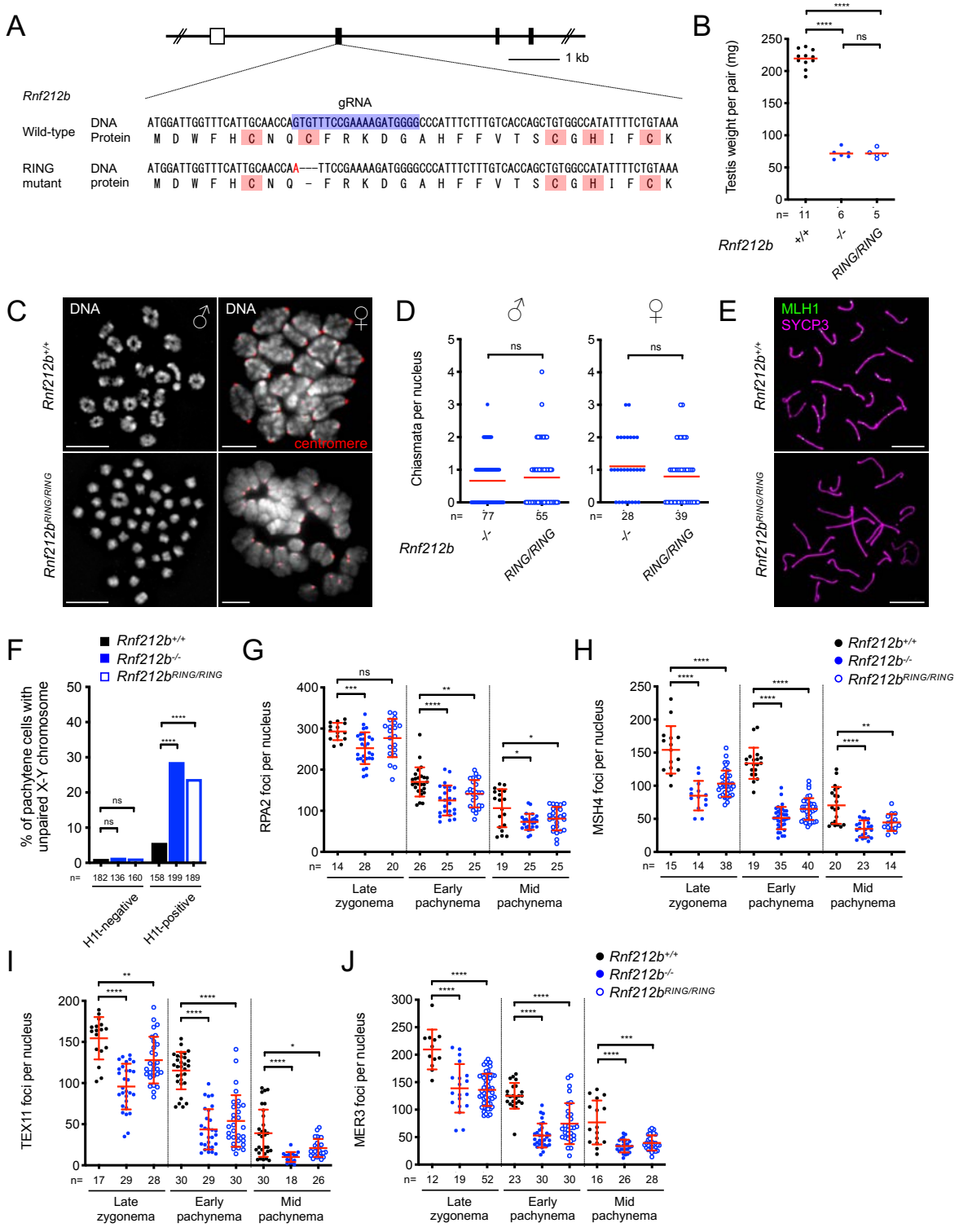

1036

1037 **Figure S10. The RING finger domain is required for RNF212B function *in vivo*, related to**

1038 **Figure 4.**

1039 (A) Scheme of the *Rnf212b* RING mutation. A three-nucleotides deletion in addition to a single-

1040 nucleotide substitution (shown in red) induced loss of the 9th cysteine residue with no change in

1041 other protein-coding amino acids. White and black boxes indicate 5' UTR and coding exons,

1042 respectively. The guide RNA (gRNA) sequence is highlighted in blue. Cysteine and histidine

1043 residues of RING finger domain are highlighted in pink.

1044 (B) Reduced testis size in *Rnf212b*$^{RING/RING}$ mutants. Red bars indicate means. ns, not significant

1045 ($p > 0.05$); ****$p \leq 0.0001$ for two-tailed *t* tests. Numbers of mice analyzed are indicated below

1046 the X axis.

1047 (C) Diminished chiasma numbers in *Rnf212b*$^{RING/RING}$ meiocytes. Left, wild-type and

1048 *Rnf212b*$^{RING/RING}$ spermatocytes in diakinesis/metaphase-I stages stained with DAPI. Right,

1049 metaphase-I oocytes from ≥2 months old wild-type and *Rnf212b*$^{RING/RING}$ females were stained

1050 with DAPI and immunostained for centromeres. Scale bars, 10 μm.

1051 (D) Chiasma counts in *Rnf212b*$^{-/-}$ and *Rnf212b*$^{RING/RING}$ meiocytes. Red bars indicate means. ns,

1052 not significant ($p > 0.05$) for two-tailed Mann-Whitney tests. Total numbers of nuclei analyzed

1053 are indicated below the X axis.

1054 (E) Absence of MLH1 foci in *Rnf212b*$^{RING/RING}$ spermatocytes. Mid-late pachytene nuclei from

1055 wild-type and *Rnf212b*$^{RING/RING}$ spermatocytes immunostained for SYCP3 and MLH1. Scale

1056 bars, 10 μm.

1057 (F) High frequency of unpaired X-Y chromosomes in H1t-positive pachytene *Rnf212b*$^{RING/RING}$

1058 cells. ns, not significant ($p > 0.05$); ****$p \leq 0.0001$ for Fisher's exact tests. Total numbers of cells

1059 analyzed from 3 mice of each genotype are indicated below the X axis.

1060 (G-J) Focus counts of RPA2 (G), MSH4 (H), TEX11 (I), and MER3 (J) in wild-type, *Rnf212b*$^{-/-}$,

1061 and *Rnf212b*$^{RING/RING}$ spermatocytes. Red bars indicate means ± SDs. ns, not significant ($p >$

1062 0.05); *$p \leq 0.05$; **$p \leq 0.01$; ***$p \leq 0.001$; ****$p \leq 0.0001$ for two-tailed Mann-Whitney tests. Total

1063 numbers of nuclei analyzed are indicated below the X axes.

Ito et al., Figure S11 (related to Figure 4)

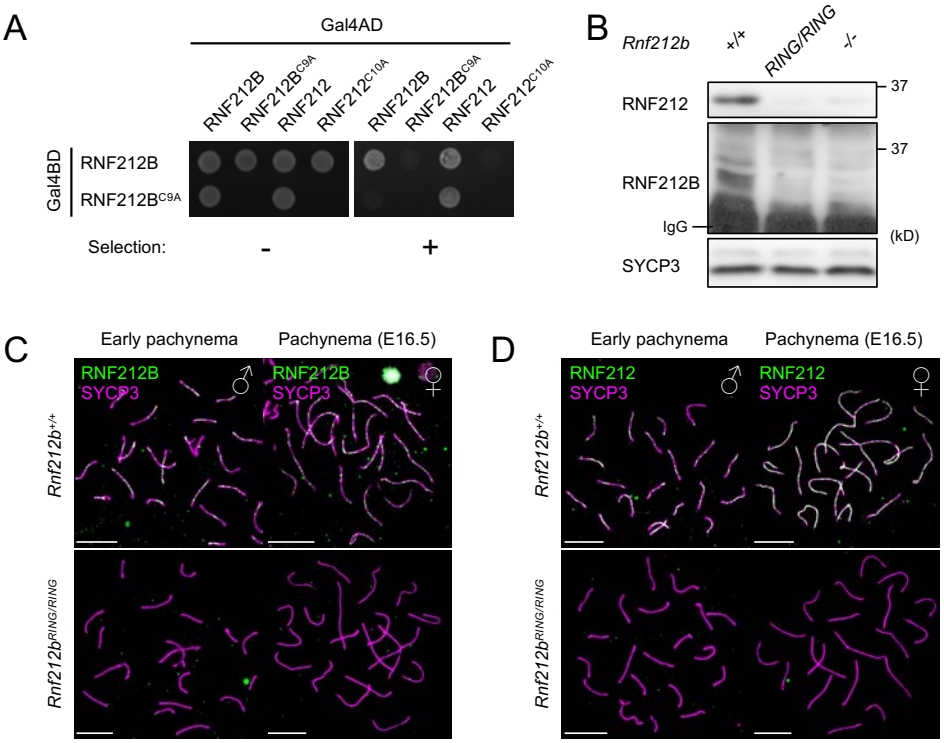

Figure S11. Role of the RNF212B RING-finger domain for self-interaction, chromosomal localization, and protein stability, related to Figure 4.

(A) Yeast two-hybrid assay shows that a C9A RING-domain mutation in RNF212B diminishes its self-interaction but not its interaction with RNF212.

(B) Diminished protein levels of RNF212B and RNF212 in *Rnf212b*$^{RING/RING}$ spermatocytes. Whole-testis extract from indicated genotypes were subjected to immunoblotting for RNF212 and IP-immunoblotting for RNF212B. SYCP3 is a loading control of meiotic cells.

(C and D) Chromosomal localization of RNF212B (C) and RNF212 (D) is diminished in

1073 *Rnf212b*$^{RING/RING}$ mutant meiocytes. Early pachytene spermatocyte nuclei from wild-type and

1074 *Rnf212b*$^{RING/RING}$ testes (left); and pachytene-stage nuclei from wild-type and *Rnf212b*$^{RING/RING}$

1075 oocytes at E16.5 (right) were immunostained for SYCP3 and RNF212B (C) or RNF212 (D).

1076 Scale bars, 10 μm.

Ito et al., Figure S12 (related to Figure 5)

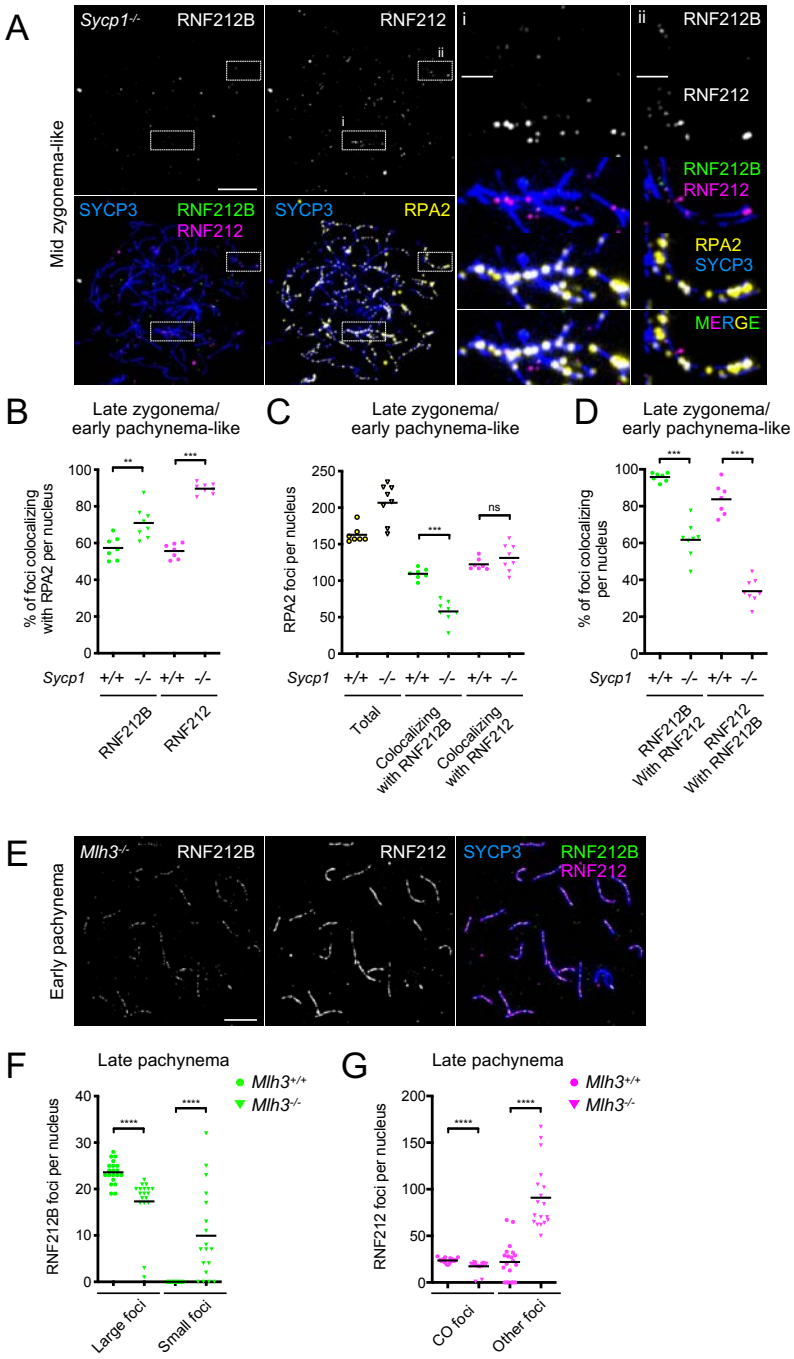

1077

1078 **Figure S12. Chromosomal localization of RNF212B and RNF212 in mutants defective for**

1079 **synapsis and crossing over, related to Figure 5.**

1080 (A) A mid zygotene-like *Sycp1*$^{-/-}$ spermatocyte nucleus immunostained for SYCP3, RNF212B,

1081 RNF212, and RPA2. General staining of RNF212B and RNF212 is absent but limited

1082 localization to small regions where homologous axes are closely aligned can be detected

1083 (magnified in the panels on the right).

1084 (B and C) Quantification of RPA2 foci colocalizing with RNF212B and RNF212. (B) Degree of

1085 RNF212B and RNF212 colocalization with RPA2. (C) Quantification of total and colocalizing

1086 RPA2 foci. Black bars indicate means. 7 early-pachytene *Sycp1*$^{+/+}$ nuclei and 8 late-

1087 zygotene/early-pachytene-like *Sycp1*$^{-/-}$ nuclei were analyzed.

1088 (D) Quantification of RNF212B-RNF212 colocalization. Black bars indicate means. 7 early

1089 pachytene *Sycp1*$^{+/+}$ nuclei and 8 late zygotene/early pachytene-like *Sycp1*$^{-/-}$ nuclei were

1090 analyzed.

1091 (E) Normal chromosomal localization of RNF212B and RNF212 in early pachytene *Mlh3*$^{-/-}$

1092 mutant spermatocyte nuclei. An early pachytene nucleus immunostained for SYCP3, RNF212B

1093 and RNF212 is shown.

1094 (F) Numbers of RNF212B and RNF212 foci in wild-type and *Mlh3*$^{-/-}$ late-pachytene

1095 spermatocyte nuclei. Left, numbers of large and small RNF212B foci. Right, numbers of

1096 RNF212 foci associated with crossover sites (colocalizing with large RNF212B foci) and other

1097 sites. Black bars indicate means. 20 *Mlh3*$^{+/+}$ and 18 *Mlh3*$^{-/-}$ nuclei were analyzed.

1098 ns, not significant ($p > 0.05$); **$p \leq 0.01$; ***$p \leq 0.001$; ****$p \leq 0.0001$ for two-tailed Mann-

1099 Whitney tests. Scale bars, 10 μm in images of full nuclei (A and E) and 2 μm in the magnified

1100 panels (A).

Ito et al., Figure S13 (related to Figures 6 and 7)

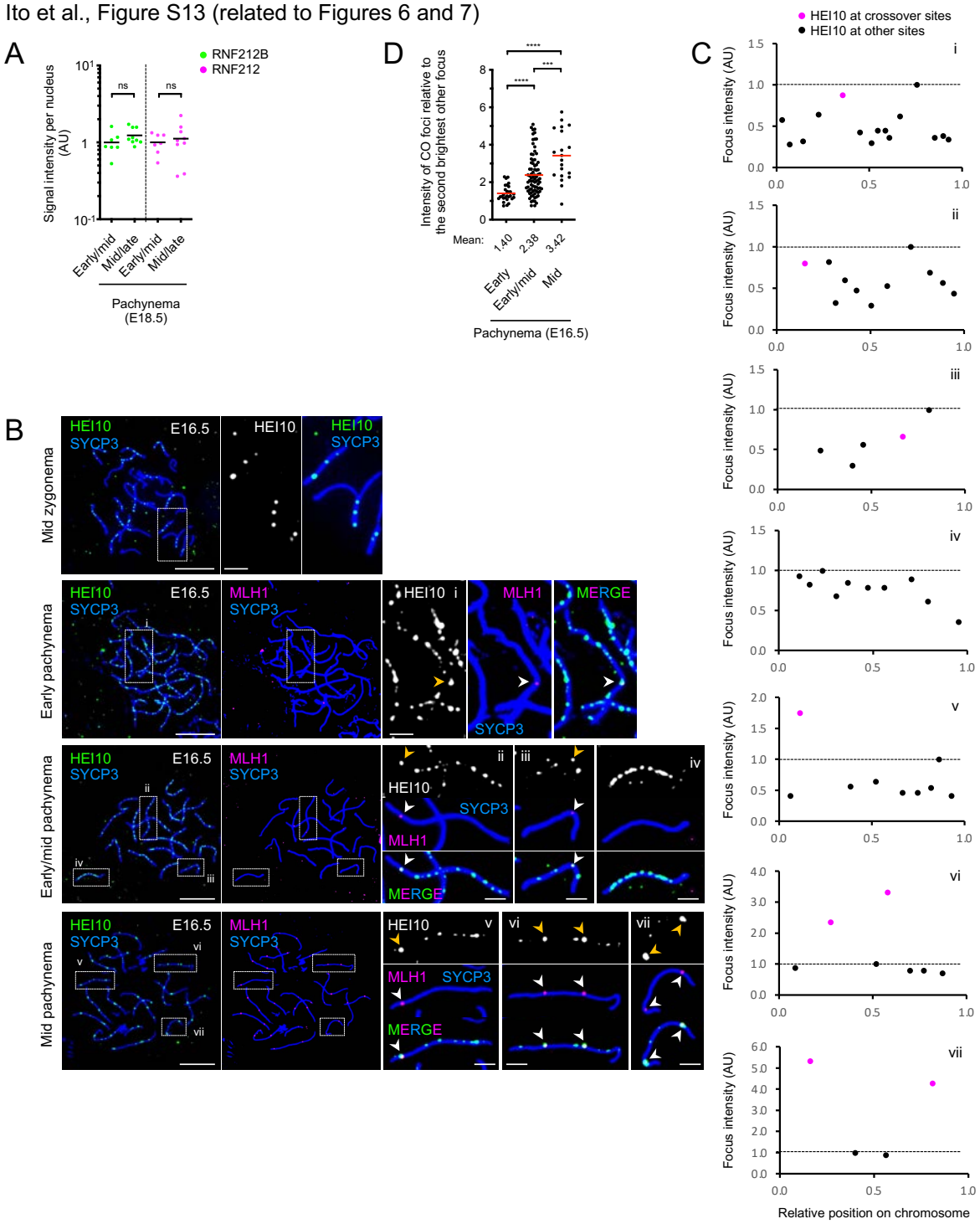

1102 **Figure S13. Localization of HEI10 and MLH1 in oocytes, related to Figures 6 and 7.**

1103 (A) Total signal intensity of RNF212B and RNF212 per nucleus in early/mid and mid/late

1104 pachytene oocytes. Black bars indicate means. ns, not significant ($p > 0.05$) for two-tailed

1105 Mann-Whitney tests. Nuclei analyzed were the same as in **Figure 6H**.

1106 (B) HEI10 localization at successive prophase-I stages of fetal oocyte nuclei from embryonic

1107 day 16.5 (E16.5). Surface-spread prophase-I oocyte nuclei in mid zygonema, early pachynema,

1108 early/mid pachynema, and mid pachynema were immunostained for SYCP3, HEI10, and MLH1.

1109 Arrowheads indicate crossover sites marked by MLH1. The magnified images show

1110 representative chromosomal regions. Scale bars, 10 μm for images of full nuclei and 2 μm for

1111 magnified panels.

1112 (C) Representations of per chromosome analysis of HEI10 foci for the chromosomes highlighted

1113 in (B). Each HEI10 focus is represented by a dot. Magenta dots indicate HEI10 foci at crossover

1114 sites (colocalizing with MLH1 foci). The dashed line indicates the signal intensity of the brightest

1115 other focus (noncrossover focus) along the same chromosome.

1116 (D) Per chromosome analysis showing that HEI10 foci located at crossover sites (colocalizing

1117 with MLH1) increase in relative intensity as pachytene progresses. Mean intensities are

1118 indicated by red lines and values shown below the graph. ns, not significant ($p > 0.05$); ***$p \leq$

1119 0.001 for two-tailed Mann-Whitney tests. 31, 91, and 105 crossover foci from 14 early

1120 pachytene, 9 early/mid pachytene, and 6 mid pachytene nuclei were analyzed, respectively.

1121

1122 **MATERIALS AND METHODS**

1123 **Mice**

1124 Mice were maintained and euthanized according to the guidelines of the Institutional Animal

1125 Care and Use Committees of the University of California Davis. All mice were congenic with the

1126 C57BL/6J background except for *Sycp1*$^{-/-}$ mutant mice. The *Rnf212*$^{-/-}$, *Hei10*$^{mei4/mei4}$, *Spo11*$^{-/-}$,

1127 *Sycp1*$^{-/-}$ and *Mlh3*$^{-/-}$ mutant lines were previously described [15, 25, 49, 51, 52]. Mature adult mice (2-6

1128 months old) were used for experiments unless otherwise noted.

1129

1130 *Rnf212b* mutant alleles were generated by The Cornell Stem Cell and Transgenic Core Facility.

1131 124 bp of DNA template for sgRNA, comprising the T7 polymerase binding site and sgRNA

1132 target sequence (5'-CCCCATCTTTTCGGAAACAC-3') followed by the remaining sgRNA

1133 sequence, were amplified by PCR as previously described [63] and purified using a GeneJET

1134 PCR Purification Kit (Thermo Scientific, K0702). 600 ng of purified DNA template was *in vitro*

1135 transcribed for 4 h at 37°C using MEGAshortscript T7 Transcription Kit (Invitrogen, AM1354).

1136 sgRNA was purified using MEGAclear Transcription Clean-Up Kit (Invitrogen, AM1908), diluted

1137 to 1.6 μg/μl and stored at -80°C prior to embryo injection. 12.5 ng/μl of purified sgRNA and

1138 either 12.5 or 25 ng/μl of Cas9 mRNA were microinjected into pronuclei of 2-cell stage of

1139 C57BL/6J homozygous embryos. Embryos were transferred to pseudo-pregnant female

1140 recipients 2 days after pronuclear injection at the 4-cell stage. Genomic DNA of founder mice

1141 was isolated from toe clips, PCR-amplified, cloned into the pCR4Blunt-TOPO vector (Invitrogen,

1142 450031), and Sanger-sequenced to identify mutations. Founder mice were backcrossed to

1143 C57BL/6J mice for ≥4 generations and heterozygous mice were bred to homozygosity.

1144 Genotyping was performed by PCR on genomic DNA isolated from mouse tails. Primers used

1145 for cloning and genotyping are listed in **Table S2**.

1146

1147 **Total RNA extraction, RT-PCR, and 5' RACE**

1148 Tissues were dissected from adult male mice, washed in phosphate-buffered saline (PBS),

1149 frozen in liquid nitrogen and stored at -80°C prior to RNA extraction. Total RNA was extracted

1150 using TRIzol according to manufacturer's instructions (Invitrogen). 1 µg of total RNA was

1151 reverse-transcribed using the SuperScript IV First-Strand Synthesis System (Invitrogen,

1152 18091050) and synthesized cDNA was PCR-amplified. For 5' RACE, 4 µg of total RNA from

1153 testes was reverse-transcribed using 5' RACE System for Rapid Amplification of cDNA Ends

1154 (Invitrogen, 18374058) and synthesized cDNA was PCR-amplified, cloned into the pCR4-TOPO

1155 TA vector (Invitrogen, K457501) and Sanger-sequenced to identify translation initiation site.

1156 Primers used are listed in **Table S2**.

1157

1158 **Yeast two-hybrid assays**

1159 Full-length mouse *Rnf212b* and *Rnf212* cDNAs were PCR amplified from mouse testis cDNA,

1160 prepared as above, and cloned into pGADT7 and pGBKT7 vectors (Clontech) using a Gibson

1161 Assembly Cloning Kit (NEB, E2611S). Full-length mouse *Hei10* coding sequence was

1162 synthesized by Twist Bioscience and cloned into pGADT7 and pGBKT7. Prey and bait vectors

1163 were co-transformed into the Y2HGold strain. Transformants were suspended in 20 µl sterile

1164 water, and 2 µl spotted onto fresh plates with and without selection: SD/-Trp/-Leu plate, SD/-Trp/-

1165 Leu containing 200 ng/ml of Aureobasidin A (Clontech, 630466) to select for the *AUR1-C* reporter

1166 gene, or SD/-Trp/-Leu /-Ade/-His to select for *ADE2* and *HIS3* reporters. After incubation of the

1167 plates at 30°C for 3 days, single colonies were inoculated into SD/-Trp/-Leu media and grown

1168 overnight. Colonies were resuspended at OD_{600} = 1, four 10-fold serial dilutions were prepared,

1169 and 10 μl drops were spotted onto selection plates and incubated at 30°C for 3 to 5 days.

1170 Primers used for cloning and point mutagenesis are listed in **Table S2**.

1171

1172 **Antibody production**

1173 Polyclonal antibodies against mouse RNF212B were raised in Guinea pigs. Codon-optimized of

1174 full-length mouse RNF212B was cloned into pET-28b (+) (Addgene) with a C-terminal 6xHis tag.

1175 *E. coli* Arctic Express (DE3) cells (Agilent Technologies Inc.) transformed with the mouse

1176 RNF212B-6xHis expression vector were grown in 2L of LB at 30°C to an OD_{600} of 0.8, and

1177 protein expression was induced with 0.5 mM IPTG followed by incubation at 11°C in media

1178 supplemented with 0.1 mM $ZnCl_2$. ~5 g of cells were pelleted by centrifugation, suspended in 60

1179 ml of denaturing lysis buffer A (6M Guanidine, 25 mM sodium-phosphate pH 7.4, 500 mM NaCl,

1180 0.1 mM $ZnCl_2$, 1 mM β-mercaptoethanol, 20 mM imidazole, 10% glycerol) and sonicated.

1181 Samples were centrifuged at 35,000 rpm in a Ti-45 rotor (Beckman) for 45 min and soluble

1182 extract was applied to a 5 ml HisTrap FF column (GE healthcare Inc.) using a GE AKTA Avant
1183 25 FPLC system. After equilibrating with 5 column volumes (CV) of lysis buffer A, followed by
1184 washes with 10 CV of wash buffer B (6M urea, 25 mM sodium-phosphate pH 7.4, 500 mM
1185 NaCl, 1 mM β-mercaptoethanol, 10% glycerol) supplemented with 60 mM imidazole, bound
1186 proteins were eluted with a linear gradient of imidazole (60-600 mM) in buffer B. Peak fractions
1187 were pooled and dialyzed extensively in decreasing urea concentrations (6M to 1M urea in 25
1188 mM sodium-phosphate pH 7.4, 500 mM NaCl, 1 mM β-mercaptoethanol, 10% glycerol). Protein
1189 concentrations were determined by Bradford and spectrophotometric (A_{280}) methods. Two
1190 Guinea pigs were immunized with purified RNF212B protein by Antibodies Incorporated (Davis,
1191 CA). The IgG fraction was purified from the resultant sera, using the Montage antibody
1192 purification kit according to manufacturer's instructions (Millipore Sigma), and dialyzed against
1193 PBS containing 10% glycerol and aliquots stored at -80°C.
1194
1195 **Histology**
1196 Testes from adult male mice were dissected, punctured with a 27-guage needle, and fixed in
1197 10% buffered formalin overnight at room temperature. Ovaries from 18 days postpartum (18

1198 dpp) female mice were dissected and fixed in 10% buffered formalin overnight at room

1199 temperature. Fixed testes and ovaries were washed in PBS twice and stored in 70% ethanol at

1200 4°C prior to embedding. Tissues embedded in paraffin were sectioned (5 μm) onto glass slides

1201 (Fisher Scientific, 12-550-15), deparaffinized, rehydrated, and incubated with antigen retrieval

1202 buffer (10 mM Sodium Citrate, 0.05% Tween-20) for 50 min at 100°C. Slides were then stained

1203 with hematoxylin and eosin (testes), or immunostained with anti-p63 antibody, as described

1204 below, and counterstained with hematoxylin (ovaries), and mounted with Permount (Fisher

1205 Scientific, SP15-100).

1206

1207 **Surface spreads of spermatocyte chromosomes**

1208 Surface-spread chromosomes of spermatocytes were prepared as described previously [64]with

1209 slight modification. Testes were dissected, the tunica albuginea removed, and adherent

1210 extratubular tissues removed by rinsing and dissociating seminiferous tubules in PBS using a

1211 pair of 25-gauge (adult) or 27-guage (juvenile) needles in a 35 mm petri dish (Corning, 430165).

1212 Dissociated seminiferous tubules were incubated in hypotonic extraction buffer (30 mM Tris-HCl

1213 pH 8.0, 50 mM sucrose, 17 mM trisodium citrate dihydrate, 5 mM EDTA, 0.5 mM dithiothreitol

1214 (DTT) and 0.5 mM phenylmethylsulphonyl fluoride (PMSF), pH 8.2-8.3) for 15-45 min at room
1215 temperature. After quickly rinsing seminiferous tubules in 100 mM sucrose, a small amount of
1216 tubules were placed in 40 µl of 100 mM sucrose on a glass depression slide. Tubules were torn
1217 to pieces using two fine forceps, and large pieces of tubular remnant were removed. The
1218 volume was increased to 40-60 µl by adding 100 mM sucrose and a cell suspension was made
1219 by pipetting. A clean glass slide (Fisher Scientific, 12-544-7) was dipped into freshly made PFA
1220 solution (1% paraformaldehyde adjusted to pH 9.2 using 1.25 M sodium borate, 0.15% Triton X-
1221 100) in a 50 ml Falcon tube, and excess solution was drained onto a paper towel. 20 µl of cell
1222 suspension was placed at the upper right corner of the slide and slowly dispersed in horizontal
1223 and vertical directions to homogeneously cover the slide. Hot tap water was added to a humid
1224 chamber and slides were slowly dried in the closed chamber overnight at room temperature.
1225 Slides were further dried for 3 hr with lid ajar, and then for 1-2 hr with the lid removed. Slides
1226 were washed once for 5 min in deionized water and twice for 5 min in 0.4% Photo-Flo 200
1227 solution (Kodak, 1464510) in a coplin jar before air-drying at room temperature. Slides were
1228 either directly processed for immunostaining, as described below, or stored wrapped in
1229 aluminum foil at -80°C prior to immunostaining. For SIM imaging, 15 µl of cell suspension was

1230 placed at the upper right corner of a coverslip (Fisher Scientific, 12-544-E) coated with 90 µl of

1231 1% PFA, 0.15% Triton X-100 solution and slowly dispersed as above.

1232

1233 **Surface spreads of oocyte chromosomes**

1234 Surface-spread oocyte chromosomes were prepared as described for spermatocytes with

1235 modifications. Ovaries from fetal females were dissected into PBS and kept on ice prior to

1236 incubation in hypotonic extraction buffer. A pair of ovaries were incubated in hypotonic extraction

1237 buffer for 10 min at room temperature, quickly rinsed in 100 mM sucrose, and placed in 50 µl of

1238 100 mM sucrose on a glass depression slide. Ovaries were torn to pieces using a pair of 25-

1239 guage needles, and large pieces of ovarian remnant were removed. The volume was increased

1240 to 40 µl by adding 100 mM sucrose and a cell suspension was made by pipetting. One half of a

1241 clean glass slide was coated with 50 µl of freshly made 1% PFA 0.15% Triton X-100, and 10 µl

1242 of cells suspension was placed at the upper right corner of the slide slowly dispersed in

1243 horizontal and vertical directions to homogeneously cover the half slide. Slides were then dried,

1244 washed, and stored as described for spermatocyte chromosomes spreads.

1245

1246 **Chromosome spreads of diakinesis/metaphase-I spermatocytes**

1247 Testes from adult male mice were dissected, tunica albuginea removed, and seminiferous

1248 tubules placed in 2 ml of hypotonic solution (1% trisodium citrate) in a 35 mm petri dish.

1249 Seminiferous tubules were torn to pieces using two fine forceps and, after adding 1 ml of

1250 hypotonic solution, 3 ml of tubule suspension was transferred to a 15 ml Falcon tube using a

1251 plastic transfer pipette (Phenix, PP-137030). Tubule fragments were allowed to settle out for 3

1252 min and the supernatant containing suspended cells was transferred to another 15 ml Falcon

1253 tube. Remnant tubule fragments in the petri dish were suspended in 2 ml of hypotonic solution

1254 and transferred to the first 15 ml Falcon tube containing tubule fragments. The mixture of tubule

1255 fragments was resuspended using a transfer pipette, tubule fragments were settled out, and the

1256 supernatant was transferred to the 15 ml Falcon tube containing the first supernatant. The

1257 mixture of supernatants was filtered through 70 μm and 40 μm Cell Strainers (Corning 352350;

1258 Celltreat, 229481) and suspended cells were pelleted by centrifugation at 900 rpm for 10 min at

1259 room temperature. Cells were fixed by adding 3 ml of freshly made fixative solution 1 (75%

1260 methanol, 25% acetic acid with 0.375% chloroform) drop-by-drop while gentle vortexing. Cells

1261 pelleted by centrifugation at 900 rpm for 10 min at room temperature, resuspended in 3 ml of

1262 freshly made fixative solution 2 (75% methanol, 25% acetic acid, chilled to -20°C), pelleted

1263 again, and resuspended in 0.5 ml of fixative solution 2. Fixed cell suspension was dropped onto

1264 a clean glass slide (Fisher Scientific, 12-544-7) from a height of 2-3 feet height using a glass

1265 Pasteur pipette in a room with >40% humidity. Slides were air-dried for 10 min at room

1266 temperature and either stained immediately with ProLong Gold or Diamond Antifade Mountant

1267 (Thermo Fisher Scientific, P36930 or P36970) containing 1 µg/ml DAPI, or stored at 4°C prior to

1268 staining.

1269

1270 **Chromosome spreads of metaphase-I oocytes**

1271 Ovaries from adult female mice without prior hormonal stimulation were dissected, follicles were

1272 punctured in pre-warmed (37°C) M2 media (Sigma-Aldrich, M7167) using a 25-gauge needle,

1273 and germinal-vesicle stage oocytes with integral cumulus cell layers were collected.

1274 Surrounding cumulus cells were mechanically removed by pipetting and oocytes were cultured

1275 in M2 media for 7 hr at 37°C. Metaphase-I oocytes were transferred into Tyrode's acidic solution

1276 (Sigma-Aldrich, T1788) to remove the zona pellucida (ZP), and ZP-free oocytes were

1277 transferred and maintained in M2 media prior to spreading. 5-10 µl of 1% PFA solution pH 9.2

1278 containing 0.15% Triton X-100 and 3 mM DTT was placed in each well of a 12-well glass slide

1279 (Electron Microscopy Sciences, 63425-05) and one ZP-free oocyte was transferred to each well.

1280 Slides were air-dried overnight at room temperature, and either directly processed for

1281 immunostaining or stored at 4°C for up to several days prior to immunostaining.

1282

1283 **Immunostaining**

1284 Slides were rehydrated with Tris-buffered saline (TBS) pH 8.0 containing 0.05% of Triton X-100

1285 (TBST) for 3 min, blocked twice with blocking buffer (1% normal goat or donkey serum, 3%

1286 bovine serum albumin (BSA), 1x TBS pH 8.0, 0.05% Triton X-100, 0.05% sodium azide) for 15

1287 min at room temperature and incubated with primary antibodies in antibody dilution buffer (10%

1288 normal goat or donkey serum, 3% BSA, 1x TBS pH 8.0, 0.05% Triton X-100, 0.05% sodium

1289 azide) in a humid chamber overnight at room temperature. Slides were briefly rinsed with TBST,

1290 washed twice with TBST for 5 min, blocked twice with blocking buffer for 15 min at room

1291 temperature and then incubated with secondary antibodies in antibody dilution buffer in a humid

1292 chamber for 1 hr at 37°C. Slides were rinsed with TBST, washed three times with TBST for 5

1293 min, washed once with Milli-Q water for 2 min, and air-dried prior to mounting with ProLong

1294 Gold or Diamond Antifade Mountant. For SIM imaging, cover slips were blocked three times for

1295 15 min prior to primary antibody incubation.

1296

1297 For metaphase-I oocytes, slides were briefly rehydrated with TBST, washed three times with

1298 TBST for 5 min, blocked twice with blocking buffer for 15 min at room temperature, and

1299 incubated with primary antibodies in antibody dilution buffer in a humid chamber overnight at

1300 room temperature. Slides were rinsed with TBST, briefly washed twice with TBST, blocked twice

1301 with blocking buffer for 15 min at room temperature, and incubated with secondary antibodies in

1302 antibody dilution buffer in a humid chamber for 1 hr at room temperature. Slides were rinsed

1303 with TBST, briefly washed with TBST, and then washed three times with TBST for 5 min. Slides

1304 were then incubated with TBST containing 5 μg/ml DAPI for 10 min at room temperature and

1305 mounted with 50% ProLong Gold or Diamond Antifade Mountant in TBST.

1306 All primary and secondary antibodies used are listed in **Table S3**.

1307

1308 **Protein blot analysis**

1309 Testes were dissected from 16-18 dpp juvenile male mice and frozen in liquid nitrogen. Five

1310 pairs of testes were homogenized in 1 mL ice-cold RIPA buffer (50 mM Tris-HCl pH 7.5, 150 mM

1311 NaCl, 1 mM EDTA, 1% NP-40, 0.5% sodium deoxycholate, 0.1% sodium dodecyl sulfate, SDS)

1312 supplemented with protease and isopeptidase inhibitors (1x Complete protease inhibitor EDTA-

1313 free, Roche, 04693159001), 1 mM PMSF, 10 mM N-ethylmaleimide, NEM) , incubated for 15

1314 min on ice, sonicated (20% duty cycle, output 2 in burts for 2.5 min), and then incubated for 15

1315 min on ice. Following centrifugation at 14,000 rpm for 15 min at 4°C, supernatants were

1316 collected as whole-testis extracts. Protein concentrations determined by Bradford assay were

1317 normalized, and samples were subjected to electrophoresis and immunoblotting. Membranes

1318 were blocked with TBST plus 2.5% non-fat milk for 1 hr at room temperature and incubated with

1319 primary antibodies overnight at 4°C. Membranes were washed three times with TBST for 10 min

1320 each, then incubated with HRP-conjugated secondary antibodies in TBST for 1 hr at room

1321 temperature. After four washes with TBST for 10 min each, HRP signal was developed using the

1322 SuperSignal West Pico Chemiluminescent Substrate (Thermo Scientific, PI-34080) and

1323 detected using an Amersham Imager 600 (GE Healthcare).

1324

1325 All primary and HRP-conjugated secondary antibodies used are listed in **Table S3**.

1326

1327 **Image acquisition**

1328 Images of surface-spread prophase chromosomes and metaphase-I chromosome spreads were
1329 acquired using a Zeiss AxioPlan II microscope with a 63 x Plan-Apochromat 1.4 NA objective
1330 and EXFO X-Cite metal halide light source, captured with a Hamamatsu ORCA-ER CCD
1331 camera and processed using Volocity (Perkin Elmer) and Photoshop (Adobe) software. SIM
1332 images were acquired using a Nikon N-SIM super-resolution microscope and processed using
1333 NIS-Elements 2 image processing software. Airyscan images were acquired using a Zeiss
1334 LSM800 with Airyscan microscope with a 60 x 1.4 NA objective and processed using ZEN
1335 imaging software (Carl Zeiss). Images of testis sections were acquired using a Zeiss Axio
1336 Imager M2 microscope with a 20 x Plan-Apochromat 0.8 NA objective, captured with a
1337 Hamamatsu ORCA-Flash 4.0 V3 sCMOS camera and processed using ZEN imaging software
1338 (Carl Zeiss). Images of ovary sections were acquired using a ScanScope digital scanner
1339 (Asperio) and processed using ImageScope software.

1340

1341 **Image analysis**

1342 Comparisons were made between animals that were either littermates or matched by age.

1343 Numbers and colocalization of foci were determined manually. *Rnf212b*$^{-/-}$, *Rnf212*$^{-/-}$ and

1344 *Rnf212b*$^{RING/RING}$ mutant analysis was blinded with respect to the genotype of the animals.

1345 Results from more ≥2 independent experiments/animals were pooled for quantification of

1346 number of foci and chiasmata. *Spo11*$^{-/-}$, *Sycp1*$^{-/-}$, *Mlh3*$^{-/-}$ and *Hei10*$^{mei4/mei4}$ mutant analysis was

1347 not blinded to genotype because phenotypes are overt. For focus intensity analyses, RNF212B

1348 and RNF212 foci along homolog axes were automatically defined by thresholding intensity on

1349 SYCP3 staining and manually inspecting images to separate any adjacent focus pairs defined

1350 as one focus. For *Spo11*$^{-/-}$ mutant analysis, synapsed regions marked by SYCP1 were manually

1351 cropped and intensities of RNF212B and RNF212 were measured. Two regions of interest (ROI)

1352 were drawn inside nuclei but adjacent to homolog axes and their average intensity was

1353 subtracted as background for each nucleus. Results from one experiment/animal among ≥2

1354 independent experiments/animals were shown for quantification of intensities.

1355

1356 Prophase-I stages were defined by SYCP3 staining (spermatocytes) and both SYCP3 staining

1357 and fetal age (oocytes) using standard criteria. Leptonema was defined by short SYCP3

1358 stretches without evidence of synapsis determined by thickening of SYCP3 staining. Zygonema
1359 was defined by longer stretches of SYCP3 with various degree of synapsis: early, mid- and late-
1360 zygonema were defined by having <25%, 25-75% and >75% of synapsis, respectively.
1361 Pachynema was defined by full synapsis of all autosomes. For spermatocytes, early pachynema
1362 was defined by extensive synapsis between the X-Y chromosomes, mid pachynema was
1363 defined by limited/end-to-end X-Y synapsis, and late pachynema was defined by
1364 decondensed/elongated X-Y chromosomes with figure-of eight configuration and thickening of
1365 SYCP3 staining at telomeres of autosomes. Diplonema in spermatocytes was defined by
1366 internal desynapsis with various degrees of residual synapsis: early, mid and late diplonema
1367 were defined by having >75%, 75-25% and<25% of synapsis, respectively. For oocytes, nuclei
1368 with unsynapsed/desynapsed chromosomes at embryonic day 15.5 (E15.5) and at 0.5 day
1369 postpartum (0.5 dpp) were defined as zygonema and diplonema, respectively. Dictyate stage
1370 was defined by short, ragged SYCP3 stretches without evidence of synapsis at 0.5 dpp.
1371
1372 For ovary sections, numbers of oocytes were manually counted for every fifth section and
1373 counts were multiplied by five to calculate the total number of oocytes per pair of ovaries, as

1374 described previously [65].

1375

1376 **Statistical analysis**

1377 Statistical analyses were performed using Graphpad Prism software v.8-9 and R version 3.5.2.

1378 Statistical parameters and tests, sample sizes, means, error bars, and standard deviations

1379 (SDs) are described in the figures and/or corresponding figure legends. Sample sizes were not

1380 predetermined using any statistical tests.

1381

1382 **Acknowledgements**

1383 We thank M.A. Handel, P. Cohen, C. Höög, J. Ward, and R.J. Pezza for antibodies; the UC

1384 Davis MCB Light Microscopy Imaging Facility and M.R. Paddy for help with SIM imaging; the

1385 Cornell Stem Cell and Transgenic Core Facility, supported in part by Empire State Stem Cell

1386 Fund Contract Number C024174, J. Schimenti and R.J. Munroe for generating *Rnf212b* mutant

1387 mice; and members of the Hunter lab for helpful discussions. M.I. was supported by a Japan

1388 Society for the Promotion of Science postdoctoral fellowship for research abroad. S.S. was

1389 supported by A.P. Giannini postdoctoral fellowship. B.N. was supported by the Howard Hughes

Medical Institute EXROP program. N.H. is an Investigator with the Howard Hughes Medical Institute.

Author contributions

M.I. and N.H. conceived the study and designed the experiments. M.I., S.L., L.H., K.L., N.L., R.M.H., R.P., C.H., and I.H. performed the experiments and analyzed the data. Y.Y. performed oocyte culture experiments and analyzed the data. S.S. and B.N. performed histological experiments and analyzed the data. D.S.K. generated anti-RNF212B antibodies. M.I. and N.H. wrote the manuscripts with input from Y.Y., S.L., S.S., and D.S.K. All authors edited the manuscript.

Competing financial interests

The authors declare no competing financial interests.

REFERENCES

1. Watanabe, Y. Geometry and force behind kinetochore orientation: lessons from meiosis.

1406 *Nat Rev Mol Cell Biol* **13**, 370-382 (2012).

1407 2. Hunter, N. Meiotic Recombination: The Essence of Heredity. *Cold Spring Harb Perspect*

1408 *Biol* **7** (2015).

1409 3. Zickler, D. & Kleckner, N. Meiosis: Dances Between Homologs. *Annu Rev Genet* (2023).

1410 4. Faisal, I. & Kauppi, L. Reduced MAD2 levels dampen the apoptotic response to non-

1411 exchange sex chromosomes and lead to sperm aneuploidy. *Development* **144**, 1988-

1412 1996 (2017).

1413 5. Hassold, T., Hall, H. & Hunt, P. The origin of human aneuploidy: where we have been,

1414 where we are going. *Human molecular genetics* **16 Spec No. 2**, R203-208 (2007).

1415 6. Hassold, T. & Hunt, P. To err (meiotically) is human: the genesis of human aneuploidy.

1416 *Nat Rev Genet* **2**, 280-291 (2001).

1417 7. Faisal, I. & Kauppi, L. Sex chromosome recombination failure, apoptosis, and fertility in

1418 male mice. *Chromosoma* **125**, 227-235 (2016).

1419 8. Hassold, T. *et al.* Failure to recombine is a common feature of human oogenesis. *Am J*

1420 *Hum Genet* **108**, 16-24 (2021).

1421 9. Wang, S. *et al.* Inefficient Crossover Maturation Underlies Elevated Aneuploidy in

1422 Human Female Meiosis. *Cell* **168**, 977-989 e917 (2017).

1423 10. Wartosch, L. *et al.* Origins and mechanisms leading to aneuploidy in human eggs.

1424 *Prenat Diagn* **41**, 620-630 (2021).

1425 11. Cole, F. *et al.* Homeostatic control of recombination is implemented progressively in

1426 mouse meiosis. *Nat Cell Biol* **14**, 424-430 (2012).

1427 12. Wang, S., Zickler, D., Kleckner, N. & Zhang, L. Meiotic crossover patterns: obligatory

1428 crossover, interference and homeostasis in a single process. *Cell cycle* **14**, 305-314

1429 (2015).

1430 13. Chelysheva, L. *et al.* The Arabidopsis HEI10 is a new ZMM protein related to Zip3. *PLoS*

1431 *Genet* **8**, e1002799 (2012).

1432 14. Cheng, C.H. *et al.* SUMO modifications control assembly of synaptonemal complex and

1433 polycomplex in meiosis of Saccharomyces cerevisiae. *Genes & development* **20**, 2067-

1434 2081 (2006).

1435 15. Reynolds, A. *et al.* RNF212 is a dosage-sensitive regulator of crossing-over during

1436 mammalian meiosis. *Nat Genet* **45**, 269-278 (2013).

1437 16. Qiao, H. *et al.* Antagonistic roles of ubiquitin ligase HEI10 and SUMO ligase RNF212

1438 regulate meiotic recombination. *Nat Genet* **46**, 194-199 (2014).

1439 17. Rao, H.B. *et al.* A SUMO-ubiquitin relay recruits proteasomes to chromosome axes to

1440 regulate meiotic recombination. *Science* **355**, 403-407 (2017).

1441 18. De Muyt, A. *et al.* E3 ligase Hei10: a multifaceted structure-based signaling molecule

1442 with roles within and beyond meiosis. *Genes Dev* **28**, 1111-1123 (2014).

1443 19. Zhang, L., Kohler, S., Rillo-Bohn, R. & Dernburg, A.F. A compartmentalized signaling

1444 network mediates crossover control in meiosis. *Elife* **7**, e30789 doi:

1445 30710.37554/eLife.30789 (2018).

1446 20. Nguyen, H., Labella, S., Silva, N., Jantsch, V. & Zetka, M. C. elegans ZHP-4 is required

1447 at multiple distinct steps in the formation of crossovers and their transition to segregation

1448 competent chiasmata. *PLoS genetics* **14**, e1007776 (2018).

1449 21. Lake, C.M. *et al.* Narya, a RING finger domain-containing protein, is required for meiotic

1450 DNA double-strand break formation and crossover maturation in Drosophila

1451 melanogaster. *PLoS genetics* **15**, e1007886 (2019).

1452 22. Wang, K. *et al.* The role of rice HEI10 in the formation of meiotic crossovers. *PLoS*

1453 *Genet* **8**, e1002809 (2012).

1454 23. Lake, C.M. *et al.* Vilya, a component of the recombination nodule, is required for meiotic
1455 double-strand break formation in Drosophila. *Elife* **4**, e08287 (2015).
1456 24. Bhalla, N., Wynne, D.J., Jantsch, V. & Dernburg, A.F. ZHP-3 acts at crossovers to couple
1457 meiotic recombination with synaptonemal complex disassembly and bivalent formation in
1458 C. elegans. *PLoS Genet* **4**, e1000235 (2008).
1459 25. Ward, J.O. *et al.* Mutation in mouse hei10, an e3 ubiquitin ligase, disrupts meiotic
1460 crossing over. *PLoS Genet* **3**, e139 (2007).
1461 26. Shinohara, M., Oh, S.D., Hunter, N. & Shinohara, A. Crossover assurance and crossover
1462 interference are distinctly regulated by the ZMM proteins during yeast meiosis. *Nat*
1463 *Genet* **40**, 299-309 (2008).
1464 27. Pyatnitskaya, A., Borde, V. & De Muyt, A. Crossing and zipping: molecular duties of the
1465 ZMM proteins in meiosis. *Chromosoma* **128**, 181-198 (2019).
1466 28. Snowden, T., Acharya, S., Butz, C., Berardini, M. & Fishel, R. hMSH4-hMSH5
1467 recognizes Holliday Junctions and forms a meiosis-specific sliding clamp that embraces
1468 homologous chromosomes. *Molecular cell* **15**, 437-451 (2004).
1469 29. Kulkarni, D.S. *et al.* PCNA activates the MutLgamma endonuclease to promote meiotic

1470 crossing over. *Nature* (2020).

1471 30. Cannavo, E. *et al.* Regulation of the MLH1-MLH3 endonuclease in meiosis. *Nature*

1472 (2020).

1473 31. Jessop, L., Rockmill, B., Roeder, G.S. & Lichten, M. Meiotic chromosome synapsis-

1474 promoting proteins antagonize the anti-crossover activity of sgs1. *PLoS Genet* **2**, e155

1475 (2006).

1476 32. De Muyt, A. *et al.* BLM helicase ortholog Sgs1 is a central regulator of meiotic

1477 recombination intermediate metabolism. *Mol Cell* **46**, 43-53 (2012).

1478 33. Zakharyevich, K., Tang, S., Ma, Y. & Hunter, N. Delineation of joint molecule resolution

1479 pathways in meiosis identifies a crossover-specific resolvase. *Cell* **149**, 334-347 (2012).

1480 34. Tang, S., Wu, M.K.Y., Zhang, R. & Hunter, N. Pervasive and essential roles of the Top3-

1481 Rmi1 decatenase orchestrate recombination and facilitate chromosome segregation in

1482 meiosis. *Mol Cell* **57**, 607-621 (2015).

1483 35. Morgan, C. *et al.* Diffusion-mediated HEI10 coarsening can explain meiotic crossover

1484 positioning in Arabidopsis. *Nat Commun* **12**, 4674 (2021).

1485 36. Fozard, J.A., Morgan, C. & Howard, M. Coarsening dynamics can explain meiotic

1486 crossover patterning in both the presence and absence of the synaptonemal complex.
1487 *Elife* **12** (2023).
1488 37. Zhang, L., Stauffer, W., Zwicker, D., A.F., D. & Crossover patterning through kinase-
1489 regulated condensation and coarsening of recombination nodules. *bioRxiv*
1490 **2021.08.26.457865** (2021).
1491 38. Kleckner, N. *et al.* A mechanical basis for chromosome function. *Proc Natl Acad Sci U S*
1492 *A* **101**, 12592-12597 (2004).
1493 39. Zhang, L., Liang, Z., Hutchinson, J. & Kleckner, N. Crossover patterning by the beam-
1494 film model: analysis and implications. *PLoS Genet* **10**, e1004042 (2014).
1495 40. Johnston, S.E., Stoffel, M.A. & Pemberton, J.M. Variants at *RNF212* and *RNF212B* are
1496 associated with recombination rate variation in Soay sheep (*Ovis aries*). *bioRxiv*
1497 **2020.07.26.217802** (2020).
1498 41. Gershoni, M. *et al.* A pathogenic variant in the uncharacterized RNF212B gene results in
1499 severe aneuploidy male infertility and repeated IVF failure. *HGG Adv* **4**, 100189 (2023).
1500 42. Kadri, N.K. *et al.* Coding and noncoding variants in HFM1, MLH3, MSH4, MSH5,
1501 RNF212, and RNF212B affect recombination rate in cattle. *Genome Res* **26**, 1323-1332

1502 (2016).

1503 43. Johnston, S.E., Huisman, J. & Pemberton, J.M. A Genomic Region Containing REC8

1504 and RNF212B Is Associated with Individual Recombination Rate Variation in a Wild

1505 Population of Red Deer (Cervus elaphus). *G3 (Bethesda)* **8**, 2265-2276 (2018).

1506 44. Johnston, S.E., Berenos, C., Slate, J. & Pemberton, J.M. Conserved Genetic

1507 Architecture Underlying Individual Recombination Rate Variation in a Wild Population of

1508 Soay Sheep (Ovis aries). *Genetics* **203**, 583-598 (2016).

1509 45. Condezo, Y.B. *et al.* RNF212B E3 ligase is essential for crossover designation and

1510 maturation during male and female meiosis in the mouse. *Proc Natl Acad Sci U S A* **121**,

1511 e2320995121 (2024).

1512 46. Bondarieva, A. *et al.* Proline-rich protein PRR19 functions with cyclin-like CNTD1 to

1513 promote meiotic crossing over in mouse. *Nat Commun* **11**, 3101 (2020).

1514 47. Ashley, T., Walpita, D. & de Rooij, D.G. Localization of two mammalian cyclin dependent

1515 kinases during mammalian meiosis. *Journal of cell science* **114**, 685-693 (2001).

1516 48. Brown, M.S. & Bishop, D.K. DNA strand exchange and RecA homologs in meiosis. *Cold*

1517 *Spring Harb Perspect Biol* **7**, a016659 (2014).

1518 49. Hinch, A.G. *et al.* The Configuration of RPA, RAD51, and DMC1 Binding in Meiosis
1519 Reveals the Nature of Critical Recombination Intermediates. *Mol Cell* **79**, 689-701 e610
1520 (2020).
1521 50. Baudat, F., Manova, K., Yuen, J.P., Jasin, M. & Keeney, S. Chromosome synapsis
1522 defects and sexually dimorphic meiotic progression in mice lacking Spo11. *Molecular cell*
1523 **6**, 989-998 (2000).
1524 51. Romanienko, P.J. & Camerini-Otero, R.D. The mouse Spo11 gene is required for meiotic
1525 chromosome synapsis. *Molecular cell* **6**, 975-987 (2000).
1526 52. de Vries, F.A. *et al.* Mouse Sycp1 functions in synaptonemal complex assembly, meiotic
1527 recombination, and XY body formation. *Genes Dev* **19**, 1376-1389 (2005).
1528 53. Lipkin, S.M. *et al.* Meiotic arrest and aneuploidy in MLH3-deficient mice. *Nat Genet* **31**,
1529 385-390 (2002).
1530 54. McMahill, M.S., Sham, C.W. & Bishop, D.K. Synthesis-dependent strand annealing in
1531 meiosis. *PLoS biology* **5**, e299 (2007).
1532 55. Palmer, N. *et al.* A novel function for CDK2 activity at meiotic crossover sites. *PLoS*
1533 *biology* **18**, e3000903 (2020).

1534 56. Holloway, J.K., Sun, X., Yokoo, R., Villeneuve, A.M. & Cohen, P.E. Mammalian CNTD1 is
1535 critical for meiotic crossover maturation and deselection of excess precrossover sites. *J*
1536 *Cell Biol* **205**, 633-641 (2014).
1537 57. Qiao, H. *et al.* Interplay between synaptonemal complex, homologous recombination,
1538 and centromeres during mammalian meiosis. *PLoS genetics* **8**, e1002790 (2012).
1539 58. Serrentino, M.E., Chaplais, E., Sommermeyer, V. & Borde, V. Differential association of
1540 the conserved SUMO ligase Zip3 with meiotic double-strand break sites reveals regional
1541 variations in the outcome of meiotic recombination. *PLoS Genet* **9**, e1003416 (2013).
1542 59. Premkumar, T. *et al.* Genetic dissection of crossover mutants defines discrete
1543 intermediates in mouse meiosis. *Mol Cell* **83**, 2941-2958 e2947 (2023).
1544 60. van der Heijden, G.W. *et al.* Chromosome-wide nucleosome replacement and H3.3
1545 incorporation during mammalian meiotic sex chromosome inactivation. *Nat Genet* **39**,
1546 251-258 (2007).
1547 61. Ghafari, F., Gutierrez, C.G. & Hartshorne, G.M. Apoptosis in mouse fetal and neonatal
1548 oocytes during meiotic prophase one. *BMC Dev Biol* **7**, 87 (2007).
1549 62. Qiao, H. *et al.* Impeding DNA Break Repair Enables Oocyte Quality Control. *Mol Cell* **72**,

1550 211-221 e213 (2018).

1551 63. Abe, H. *et al.* The Initiation of Meiotic Sex Chromosome Inactivation Sequesters DNA

1552 Damage Signaling from Autosomes in Mouse Spermatogenesis. *Curr Biol* **30**, 408-420

1553 e405 (2020).

1554 64. Bassett, A.R., Tibbit, C., Ponting, C.P. & Liu, J.L. Highly efficient targeted mutagenesis of

1555 Drosophila with the CRISPR/Cas9 system. *Cell Rep* **4**, 220-228 (2013).

1556 65. Peters, A.H., Plug, A.W., van Vugt, M.J. & de Boer, P. A drying-down technique for the

1557 spreading of mammalian meiocytes from the male and female germline. *Chromosome*

1558 *Res* **5**, 66-68 (1997).

1559 66. Di Giacomo, M. *et al.* Distinct DNA-damage-dependent and -independent responses

1560 drive the loss of oocytes in recombination-defective mouse mutants. *Proc Natl Acad Sci*

1561 *U S A* **102**, 737-742 (2005).

1562

1563